Novel Combination of LCoS and Temporal Phase Unwrapping for 3D Shape Reconstruction.

Christhian Adonaí González Valdez

A Thesis Submitted in Partial Fulfillment
of the Requirements for the Degree of
Master of Science
in
Optics

November 15, 2007
León, Gto. México

Abstract

Recent developments on Spatial Light Modulator systems based on reflective liquid crystal microdisplays have allowed the technologies of Liquid Crystal over Semiconductors (LCoS).The highest potential of the Spatial Light Modulators is that they have dynamic addressable diffractive elements that can be used for projection purposes in multimedia projectors, High-definition television, and for experimental purposes on laboratory. However, the projecting capabilities should be tailored for specific applications, and its performance should be assessed depending on the particular application.

In industry today, the use of tactile point measuring principles are changing in favor of optical non-contact field measuring techniques, this open a new field in the research area of optical metrology which purpose is the application of techniques such as speckle interferometry, Moiré and fringe projection as a way to solve real industrial problems. 3D shape measurement has been performed in the last decades using fringe projection schemes. A recently developed method that uses projected fringe patterns is the temporal phase unwrapping (TPU) in which fringes of varying pitch and phase are projected and acquired sequentially in time. The advantage of this method with respect to the traditional spatial phase unwrapping, is the evaluation of the phase in each detector element independently from the other detector counterparts. Hence, phase errors become isolated in the image, and do not influence the result of their neighbors. However, shadows and low intensity reflected from the specimen under investigation could cause errors into the final unwrapped

phase. Noise immunity in the TPU has been studied and solved by using branch cut surfaces[1].

The combination of phase extraction methods with quality maps for phase unwrapping has been proposed previously. Bone[2] first incorporates the concept of phase quality into spatial phase unwrapping by means of a quality mask. This was followed by different approaches in terms of further algorithms based on quality maps[3, 4, 5]. To avoid the spatial unwrapping errors, we use the TPU and extrapolated the quality map application to avoid shadows and low modulation pixels. A threshold value in the histogram of the quality map allows to select areas of high visibility in which the temporal phase unwrapping algorithm can be successfully applied. The combined techniques allow noise cancellation and the study of illumination areas obtained with the fringe projection schemes.

In both configurations, we propose to isolate the non-modulating pixels using a quality map and a threshold value, that is selected from the histogram of the quality map. The novelty of this work comes from the implementation of the TPU using an LCoS device. In this work we consider the LCoS adequacy as a projection system in two configurations, the first one to generate phase holograms and the second as a conventional projecting system.

Acknowledgments

I would like to thank my supervisor Dr. Abundio Dávila Alvarez who introduced me in the science world and his invaluable supervision of this thesis. He encourage me and gave me professional support.

I thank Ing. Juan Antonio Rayas, Dra. Amalia Martínez, Dr. Miguel Torres Cisneros, Lic. Guillermo Garnica, Dr. David Moreno, Dr. Jorge Luis Marquez, Dr. Ricardo Flores, Dr. Norberto Arzate, and Dr. Jesus Moya for their helpful, friendship and interest in my professional development.

I acknowledge the support of Centro de Investigaciones en Óptica, and all the attention that I receive from Lic. Guillermina Muñíz and Dr. Francisco Cuevas to carry this project to good end.

Last but not least, I want to say thanks to all my friends for their patient and support during the complementation of this thesis.

Christhian Adonaí González Valdez.
November 2007

Contents

List of Figures

List of Tables

Chapter 1

Spatial Light Modulator LCoS

LCoS or LCOS is the abbreviation for Liquid Crystal on Silicon, and can be interpreted as a hybrid between LCD (liquid crystal display) and DLP (digital light processing). The DLP was invented by Dr. Larry Hornbeck of Texas Instruments in 1987[6] and uses tiny mirrors, one for each pixel, to reflect light coming from a lamp which is modulated by tilting the mirrors either into or away from the lens path to form an image onto a screen; it is therefore a reflective technology. LCD uses liquid crystals, one for each pixel on glass panels, light passes through these LCD panels on the way to the lens and is modulated by the liquid crystals as it passes; thus it is a transmissive technology.

LCoS combines these two ideas[7] in a reflective technology that uses liquid crystals instead of individual mirrors, a cross section diagram of an LCoS panel is shown in Fig. 1.1. In LCoS, liquid crystals are applied to a reflective mirror substrate. As the liquid crystals open and close, the light is either reflected from the mirror below or blocked, this modulates the light and creates the image. LCoS has found its principal commercial applications in projectors and RPTV (rear projection television), nowadays we can find products in the state of the art as JVC DLA-H10KS LCoS projector with a 2,500:1 contrast ratio and a resolution of 2048 x 1536 pixels, Cinetrons HD-900 projector with 6000:1 contrast ratio and 1920 x 1080 pixels of resolution and Olevia RPTV 65-inch

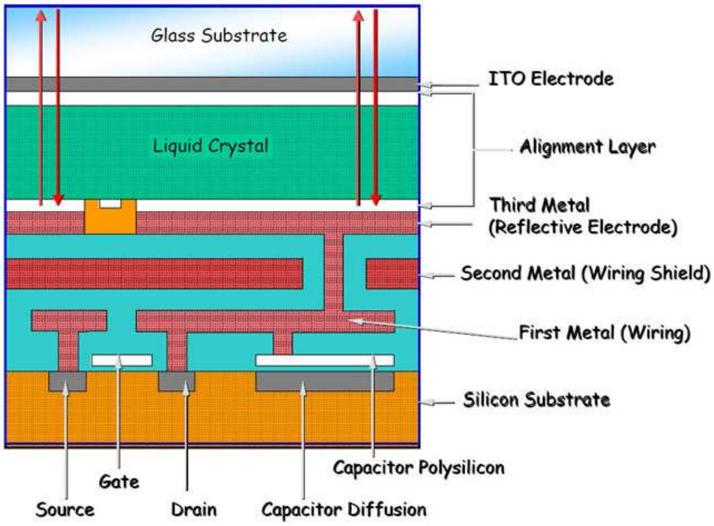

Figure 1.1: LCoS D-ILA cross section diagram, courtesy of JVC Professional Products.

with 2000:1 contrast ratio. A new technology from SONY called SXRD (silicon X-tal reflective display)[8] uses an architecture in which the silicon backplane contains the driving circuitry that controls the liquid crystal matrix, normally this would be routed between the pixels, creating a grid pattern which is visible as the screen door effect in the image itself. Without this grid of control circuitry, the tiny 8.5μ m pixels can be very close together just 0.35μ m apart. The result is a picture with a contrast ratio 10,000:1.

LCoS projectors have several key advantages over the more popular technologies. First and most important, due partly to inherent high resolution, and partly to high fill factors (minimal space between pixels) on the chips, visible pixelation on an LCOS machine is nonexistent. Second, with LCoS the pixel edges tend to be smoother compared to the sharp edges of the micro-mirrors in DLP. This gives them an analog like response, whereas micro-mirrors add high frequencies that accentuate their digital nature. This gives the LCoS image a smoother, more natural look and feel. Third, the absence of a color wheel means there is no chance to observe rainbow artifacts, eye-strain, or

Specifications for 1920x1080 LCoS				
	Brillian[9]	JVC Consumer[10]	SONY[8]	Holo Eye
LCoS Technology	Gen II LCoS	D- ILA	SXRD	Reflective LCoS microdisplay
Contrast Ratio	>6000	>5000	>5000	<1000
Panel Size	0.7 inch	0.7 inch	0.61 inch	NA
Pixel Pith	8.1μ m	8.1μ m	7μ m	19μ m
Inter pixel gap	0.4μ m	0.45μ m	0.35μ m	NA
Fill Factor	90%	89%	90%	93%
Device Control	Analog Voltage	Pulse with Modulation	Analog Voltage	Analog Voltage
Signal Level	12 bits	10.5 bits	NA	8 bits
Rise Time	4ms	2ms	2.5ms	NA
Fall Time	4ms	5ms	2,5ms	NA
Response Time	8ms	7ms	5ms	NA

Table 1.1: Lists of specifications supplied by each manufacturer for their higher technology 1080 LCoS.

headaches that some people can be susceptible to when viewing single-chip DLP projectors.

The primary weakness of LCoS technology was contrast. Currently most LCoS products are rated in the range of 500:1 to 800:1. So they do not have the contrast performance that most DLP products are able to achieve, the use of the new high contrast screen materials helps offset this weakness to some degree. Many LCoS projectors also have limited lamp life in the 1000 to 1500 hour range and on certain models lamp replacements can be much more expensive than they typically are with LCD or DLP projectors.

The LCoS is a relative new technology that provides highest resolution and each manufacturer has their own proprietary implementation and all give their version a special marketing name, some of them are listed in Table (1.1).

The Panel Contrast Ratio is probably the most critical value in the table because its determine how a signal can be sampled. The Pixel Pitch is the center to center spacing for pixels in the panel, and the Inter Pixel Gap is the inactive space between them. The Fill Factor, sometimes called the Aperture Ratio, is the percentage of the pixel area that is active, which is close to 100 percent, so the gaps between the pixels on the screen are generally not noticeable.

The Response Time is an industry standard that specifies the total time that it takes a pixel to make a transition from black to white, the Rise Time or Ton, plus the time to make a transition from white to black, the Fall Time or Toff. Response Time is one measure of how quickly the image can be changed and provides some indication of the likelihood of visible motion smear in moving images.

In summary the LCoS is an electronic device used as a display element in video projector, during the last decade it have been widely improved. This allow the use of the LCoS in the research field as a spatial light modulator (SLMs), programmable optical devices[11, 12, 13], adaptive optic[14, 15], digital holographic and difractive optics elements[16] (DOE).

1.1 Inside of a Spatial Light Modulator

The spatial light modulator is formed of liquid crystal material sandwiched between two conductive films, one of this film is a transmissive window and the other is pixelated and electrically addressable[17, 18]. The most common liquid crystal used in this optical devices is twisted-nematic liquid crystal with an helical structure, in this kind of material, the molecules tend to be parallel aligned but their positions are fully random, this means, there is an orientation order but no a positional order.

The second conductive film that is addressable will help to generate an electric field that is individually generated through the liquid crystal material (each pixel), this allow to change the effective refractive index of the liquid crystal. In this manner selective phase change may be imparted to a wavefront transmitted through the liquid crystal material according to the induced phase retardation caused by the array of pixels[19]. To produce an image, a polarized light source is focused over the LCoS, the brightness of each pixel is controlled by varying the electric field at its location; this rotates the local light polarization, and with the help of a polarizing filter the portion that has been rotating is blocked.

As is mentioned before, each manufacturer has their own proprietary implementation but in fact the basic idea is the same, Fig. 1.1 illustrate the elements and structures used in an embodiment of a reflective spatial light modulator. A transparent electrode as indium-tin-oxide (ITO) is deposited onto a glass substrate. Alignment layers formed from materials such a polymide (organic alignment layer) are applied by spin coating, a procedure used to apply uniform thin films onto flat substrates to achieve high contrast and high-speed response[20]. The purpose of alignment layers are to create a weak anchoring force that is used to align the liquid crystal molecules that are sandwiched between them. The helical structure is shown in Fig. 1.2, molecules (B1, B2) rotate around the cone and form a helix between smectic layers. The separation between alignments is designed to be thin and the surface anchor force is strong, the combined forces suppresses the helix and results in two eigen positions for the liquid crystal molecules, this make possible that the molecules switch between far ends of the cone when an electric field is applied and as a result of this the light is modulated, there are different methods for building and applying electrical fields[21, 22] with the purpose of increase the modulation capacity of the LCoS.

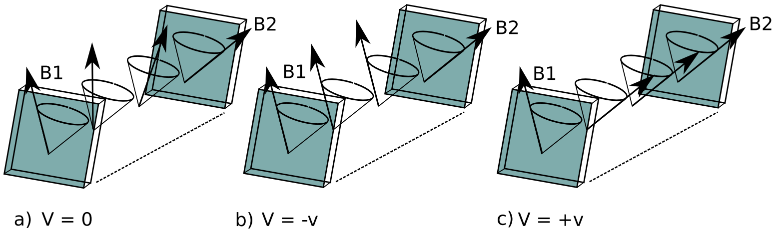

Figure 1.2: a) molecular helical structure, b) molecules rotate -V, c) molecules rotate +V, where ± V is the applied voltage to produce a rotation in the molecules.

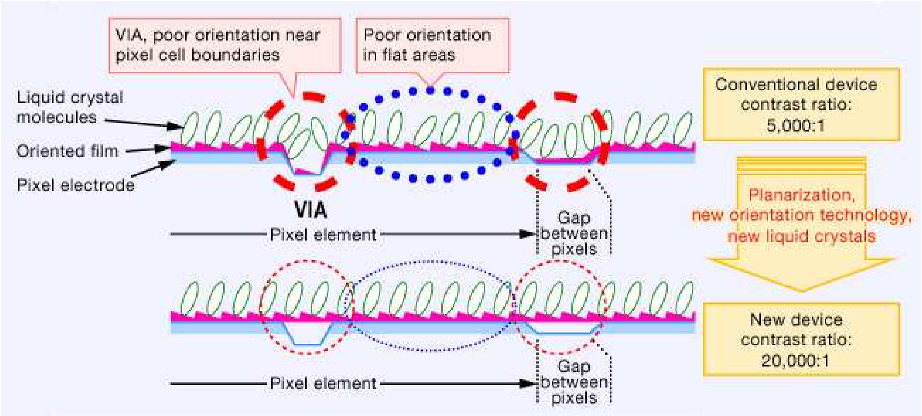

Figure 1.3: New manufacture process for increasing the contrast ratio used in JVC D-ILA, courtesy of JVC.

The LCoS suffer from surface irregularities that are unavoidable using normal semiconductor manufacturing processes, discontinuities between individual pixel cells or where the pixel cells are connected with the underlying semiconductor structure disturb the orientation of the liquid crystals, resulting in a deviation of the light from the desirable course Fig. 1.3. New developments in the manufacture process have been adopted to ensure extreme planarization; this reduces to an absolute minimum such stray light, this new technologies have realized the extremely high device contrast ratio of 20,000:1, and at the same time halved response time from 8ms to 4ms[23].

Finally, as part of the optical system used for the projection, a polarizer is used for increasing the contrast; the input light that cover the liquid crystal display is essentially unrotated, there is no change in its polarization, when the voltage source provides a voltage, the reflected light emerging from the liquid crystal is rotated, when this light passes trough the polarized[24, 25] a quantity is blocked reducing to an absolute minimum the amount of stray light reaching the imaging lens during dark scenes.

Chapter 2

Optical Techniques for Shape Measurement

2.1 Optical Shape Metrology

Conventional methods of measuring physical parameters include the requirement for contact with the object under test and the localized measurement area. In general, large numbers of separated measurement areas are required to build up an overall picture of the physical parameters, however, when the required number of sensors exceeds $10^2 - 10^3$ the cost typically becomes prohibitive. Optical techniques are increasingly becoming useful tools for precision measurement in research and for industrial applications. The field of optical metrology encompasses a large number of techniques allowing direct or indirect measurement of diverse physical quantities. A particular focus is given here on "whole-field" techniques, which provide direct measurement on a large number of points in a limited number of steps. Examples of application include measurement of shape, deformation, strain, refractive index, etc.

The optical techniques are suitable tools for the measurement of shape and deformation in different kind of objects (smooth or rough), each of the techniques has different sensitives ranging from the decimeter to the nanometer. For example coherent optical methods are well suited for applications requiring high precision for surface profile measurement, incoherent optical methods can also provide very practical solutions, and are particularly suitable for profiling applications where large surface height variations and discontinuities are encountered. In the domain of shape evaluation, classical interferometry is used for high precision such as flatness testing while structured light as moiré and fringe projection techniques are less sensitive and thus better for 3D description of deep surface and their position in space.

Most surface profiling systems trade off measurement accuracy for dynamic range, however, there is a recognized requirement in industry for optical techniques than provide both high dynamic range and high precision. Applications for these systems include automated manufacturing, vehicle guidance, line inspection, quality control, robotic vision and solid modeling and recognition issues[26].

Other important point in the industry is the whole view of the object (360^o)under test, the global coordinate system is set up and local coordinates systems are registered during measurement. A structured light imaging system is placed at an appropriate position to measure 3D shape from recording different views, and the absolute phase value at each object point is calculated. These phase value and the geometric model of the measurement system determine the local 3D coordinates of the object points. Precise transformation of these object points is required to accurately characterize the complete surface.

All the techniques presented in this chapter require, at least, a light source that illuminates the object under study and a detector capable of recording the light that is reflected, diffused or diffracted by the object. The advantages of this techniques are:

- They are non destructive.
- They have in general high resolution.
- They allow a whole field inspection.

The purpose of this section is to provide the reader with an insight into the existing optical techniques for 3D shape measurement:

- Computer vision.
- Photogrammetry.
- Contouring speckle interferometry.
- Low coherent interferometry.
- Fourier transform speckle profilometry.
- Spectral interference microscope.
- Coaxial coimage plane projection and observation profilometry.
- Laser scanning.
- Binary coding of projected structured light.
- Spatial frequency scanning of projected structured light.
- Multiplexed spatial frequency of projected structured light.
- Other Techniques.

The goal is to introduce the basic concepts of similar techniques related to this work. A particular emphasis will be placed on the temporal phase unwrapping technique, which is the base for the development of the this work.

2.2 Computer Vision

Computer vision techniques are based in the analysis of a scene or image, the main problem is to obtain depth information directly from two dimensional intensity images, in general the recovery process requires the knowledge of the objects in the scene and the projection geometry.

We can make use of the shape, density and size of the primitives textures in the object to obtain information about surface orientation and surface profile, this technique is commonly named "shape-from-texture[27]"; this technique has several problems such as projective distortion, unpredictable natural textures that does not allow to model their precise geometry, and assumptions of the texture regularity that are not formally adequate. More over, the detectors must be able to resolve the surface texture, in practice the technique is only suitable for simple surfaces.

Other important technique in computer science is the "stereo vision", in which two cameras are displaced from each other by a known distance. A feature in the scene is captured by each camera in its own view, as the image plane in the cameras are coplanar, depth information can be recovered by identifying the disparities of corresponding image points. There are a lot of works in which this technique is applied [28, 29].

A basic technique known as "shape from shading"[30, 31], uses a single light source, when a diffuse surface is illuminated by a point source, the lines of constant intensity can be expressed by a second order polynomials, the intensity variations in the image due to changes in surface slope can be used to determinate to find out the surface position and orientation; "Photometric stereo"[32, 33] extends the technique by using several light sources, a minimum of three independent point sources is therefore required to obtain a set of equations and obtain intersections of this curves to define the surface orientation.

2.3 Photogrammetry

Photogrammetry relies on the overlapping of photographs for the extraction and the analysis of three dimensional information[34, 35]. Photogrammetry

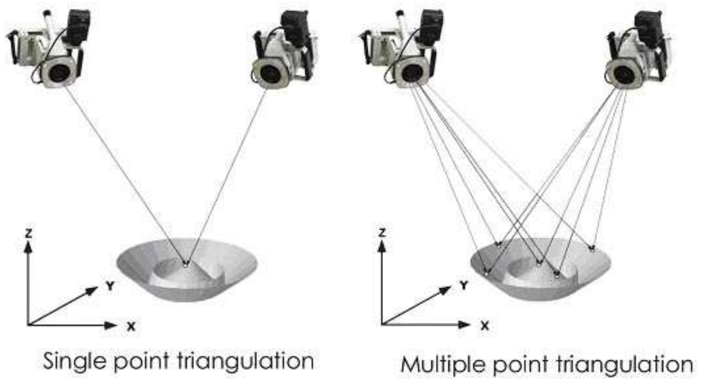

Figure 2.1: Triangulation principle in photogrammetry.

typically is applied to the stereo vision method and developed almost to exclusively for mapping large geometrical areas in the domain of civil engineer and remote sensing. The relative geometrical orientation of the overlapping photographs permit the reconstruction of a hypothetical three dimensional stereo-model which is then used to measure the size, shape and location of the objects. In general, three dimensional reconstruction is based on the "bundle adjustment principle"[36], the precise location of the point can be determined using triangulation geometry by the intersection of converging lines in space Fig. 2.1, the optimal solution is found using a least square minimization approach. To determinate the scale, a single distance in the object must be know, in general markers must be attached to the test surface as homologous points to aid in solving the correspondence problem unambiguously.

2.4 Contouring Speckle Interferometry

2.4.1 In-Plane Configuration

The optical setup shown in Fig. 2.2 gives the fringes which are sensitive to in-plane displacement. The object is illuminated by two plane wave fronts

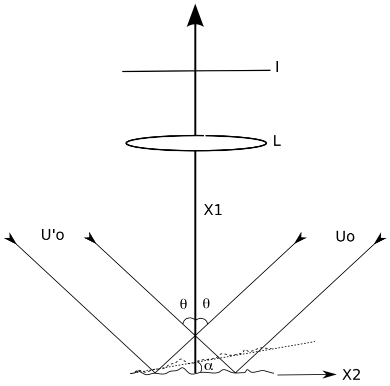

Figure 2.2: Schematic Diagram: The in plane displacement arrangement of speckle pattern correlation interferometer for contouring by object tilting.

inclined at equal opposite angle θ. The two speckle wavefront from each beam arrive to the camera at the image plane, thus for each point in the object there are two rays that interfere in the image plane, the total sum of points over the entire object results in a speckle pattern[37].

The relative phase of the two incident wavefronts is constant over planes parallel to $x1$, displacements in this plane will not introduce a relative phase change. Kaifu Wang was reported that only the first order derivative component has an influence on curvature fringe formation and the second order derivative components have no influence on curvature fringe formation. The phase change of the two beams can be expressed as:

$$\Delta\phi = \frac{4\pi}{\lambda}\sin(\theta)u\,, \tag{2.1}$$

where λ is the wavelength of the light and u is the displacement component in the $x2$ direction. The formation of fringe pattern is based on a correlation principle. The incremental displacement between two adjacent fringes is $\frac{\lambda}{2\sin(\theta)}$, thus the method can measure very small displacements and the sensitivity can be reduced by varying the angle θ, the limit in the maximum measurable displacement will be imposed by the speckle size.

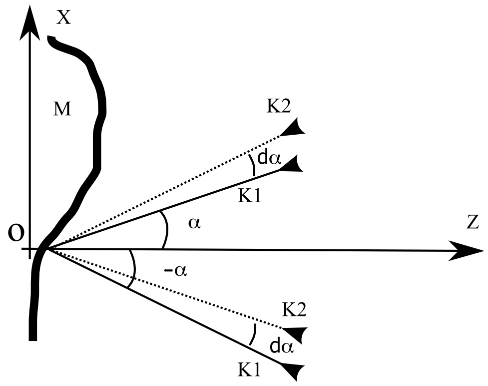

Figure 2.3: Schematic Diagram: Contouring Speckle Interferometry in plane illumination tilted an angle $d\alpha$.

The sensitivity depends on the angle of illumination, and the angle of tilt α. For large illumination angles, the equation for the fringes of constant depth reduces to a simple form as[38, 39]:

$$\Delta h = \frac{\lambda}{2\alpha \sin(\theta)}\,, \tag{2.2}$$

Speckle interferometry is most often encountered in applications such as surface displacement analysis, several methods, based on this technique have been developed for measuring surface profile, this could be possible by the variation of parameters such as: illumination direction, temporal coherence and optical wavelength.

The purpose of changing the illumination directions is to perform shape measurement on rough objects, using an interferometer similar to the used in-plane measurement. However, as there is no loading of the object, the fringes are produced by rotation $d\alpha$ of the two illumination beams in the same direction.

Let's call $\triangle\varphi_o$ the total geometrical phase difference between the two symmetrical beams that illuminate the point O Fig. 2.3. The corresponding phase difference for a different point $M(x, z)$ is:

$$\triangle\varphi_M = \triangle\varphi_o + \frac{2\pi}{\lambda}(K_1 - K_2)\bar{OM}\,, \tag{2.3}$$

to simplify, we assume that the beams rotate by an angle $d\alpha$ around the point O. If the rotation axis is somewhere else, which is usually the case in a real set-up, an additional phase constant is introduced at every point of the interferogram. As $d\alpha$ does not change after rotation, for the point M, the new phase difference is given by Equation (2.3) with the new vector K_1 and K_2. If $d\alpha$ is small, we obtain the total phase change between the two expositions for the point M as:

$$\triangle\varphi = \frac{2\pi}{\lambda}2z\sin\alpha\sin d\alpha\,, \tag{2.4}$$

the sensitivity to the z coordinate is:

$$s = \frac{\lambda}{2d\alpha\sin\alpha}\,, \tag{2.5}$$

the highest sensitivities are in the range of a few tens of λ. It is possible to obtain higher resolutions by accumulating successive $d\lambda$ increments which also cancels decorrelation effects. The speckle contouring technique competes with fringe projection, as both methods provide the same kind of sensitivities. Its main advantage is that it can be easily integrated with an in plane speckle interferometer. Rodriguez Vera[40, 41] provide a useful state of the art review of electronic speckle contouring (ESC) method.

2.4.2 Out-Plane Configuration

When the light source is displaced by an angle $\Delta\alpha$ carrier fringes are generated over the flat plane along the X axis in an out-of-plane speckle interferometer, Fig. 2.4. The pitch of the linear carrier fringes have a frequency given by[42, 43]:

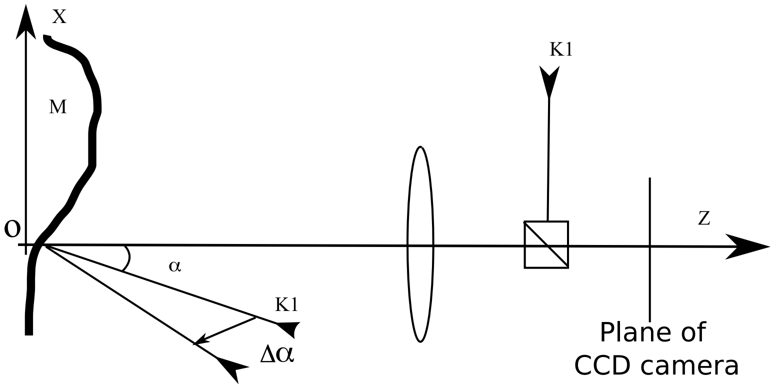

Figure 2.4: Schematic Diagram: Contouring Speckle Interferometry out plane illumination.

$$f_x = \frac{\cos(\alpha)\sin(\Delta\alpha)}{\lambda}\,, \tag{2.6}$$

If a 3D shape is used instead of a plane, it modulates the carrier fringes and the phase extraction methods available for carrier fringes can be applied to extract the depth information represented by:

$$z(x,y) = \frac{\lambda\phi(x,y)}{2\pi\sin(\alpha)\sin(\Delta\alpha)}\,, \tag{2.7}$$

The carrier fringes can be also generated by displacement of the reference beam, the number of fringes and the sensitivity in both cases can be controlled by altering the angle $\Delta\alpha$ and the illumination angle α.

2.5 Low Coherence Interferometry

Temporal coherence interferometry describes the correlation between a wave with itself as a function of the distance along the direction of propagation, the degree of coherence can be determinate from the fringe contrast, for waves of equal intensity, the degree of coherence is equal to:

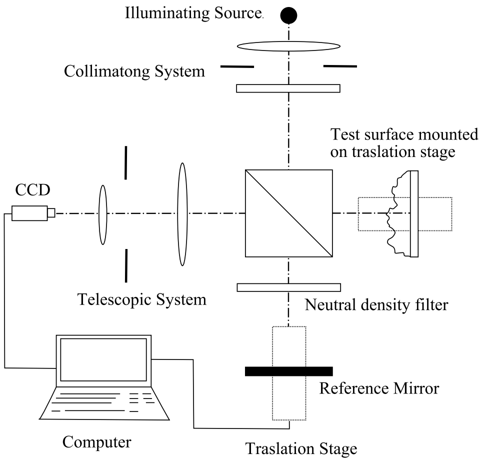

Figure 2.5: Optical arrangement for low coherence interferometry.

$$V = \frac{I_{max} - I_{min}}{I_{max} + I_{min}}, \tag{2.8}$$

where I_{max} and I_{min} are the maximum and minimum intensity, respectively. By using the system described in Fig. 2.5 it is possible to evaluate the profile of some surfaces with resolution of around 0.1 microns, depending on the light source adopted (short coherence length) typically a laser diode, a LED, or incandescent lamp.

The arrangement Fig. 2.5 is based on a Michelson interferometer with one of the mirrors replaced by the test surface. At the beginning of the procedure, the reference mirror is positioned closer to the beam-splitter than the object surface. By moving the mirror step by step away from the beam-splitter, the reference plane scans the object surface: every speckle on the surface modulates only when the difference of optical paths between the reference and the object surfaces is within the coherence length of the used light.

The short coherence length restricts interference to those speckles that correspond to the surface elements close to the plane of the object under test being analysis, where the optical path lengths of the interferometer arms balance. The CCD pixels are labeled by integer pairs (i, j) and the corresponding intensity values at the N-th translation step are denoted by $I_N(i, j)$. The absolute values of the difference $I_N(i, j) - I_{N-1}(i, j)$ is calculated for each pixel and compared with a reference value I_s. More precisely, for those pixels such that:

$$\mid I_N(i, j) - I_{N-1}(i, j) \mid > I_s\,, \tag{2.9}$$

at the end of the translation process of the reference mirror, to every pixel correspond a value related to the last step for which condition Equation (2.9) was fulfilled. From this profile map the 3D surface of the object could be simulated. To obtain a good profile map the speckle contrast variations at each step must be greater than the camera noise: a proper choice of the threshold value I_s can eliminated the camera noise as well as small intensity fluctuations of the illuminating beam.

2.6 Fourier Transform Speckle Profilometry

Fourier transform speckle profilometry[44] (FTSP) is based on the combination of wavelength-shift speckle interferometry and the Fourier transform technique (FFT) for temporal fringe pattern analysis. The optical arrangement Fig. 2.6 is similar to the used in Sect. 2.5 but with a coherence frequency tunable laser diode as the light source.

The basic technique scans the laser diode injection current, the wave number is giving by $k(t) = \alpha * t + \kappa(t)$ varies quasi-linearly with time, where α is a constant and $\kappa(t)$ represent the initial wave number $\kappa(0)$. This wavelength scanning causes the the speckle intensity vary sinusoidally as:

$$g(x, y, t) = a(x, y, t) + b(x, y, t)\cos(2k(t)l(x, y))\,, \tag{2.10}$$

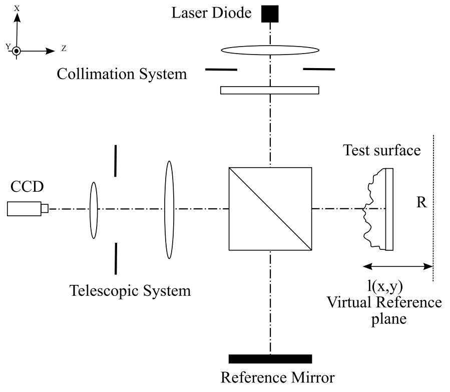

Figure 2.6: Optical arrangement for Fourier transform speckle profilometry.

where $l(x, y)$ is the optical path difference, $a(x, y, t)$ and $b(x, y, t)$ are respectively the background intensity and the fringe amplitude that change with the injection current. The amplitude and phase modulation are given by:

$$g(x, y, t) = a(x, y, t) + b(x, y, t)\cos(2\pi f_0(x, y)t + \phi(x, y, t))\,, \tag{2.11}$$

where

$$f_0(x, y) = \frac{\alpha l(x,y)}{\pi} \tag{2.12}$$

and

$$\phi(x, y, t) = 2\kappa(t)l(x, y)\,, \tag{2.13}$$

the FFT provides a method for extracting the height information encoded in the temporal carrier frequency. If we let $c(x, y, t) = \frac{1}{2}b(x, y, t)e^{i\phi(x,y,t)}$ the Fourier transform of $g(x, y, t)$ with respect to t id given by[45]

$$G(x, y, f) = A(x, y, f) + C[x, y, f - f_o(x, y)] + C^*[x, y, -f + f_o(x, y)]\,, \tag{2.14}$$

where * denotes the complex conjugate. As the separation of these spectra is proportional to $l(x, y)$ it is necessary to arrange the interferometer with a large optical path difference between arms to enable the spectra to be separated. Finally one of the side bands is selected by filtering and the inverse Fourier transform computed to obtain $c(x, y, t)$[46]. Finally, one dimensional phase unwrapping along the time is required to recover $\phi(x, y, t)$ and thus obtain the height information.

2.7 Spectral interference microscope

The spectral interference microscope[47] is based in a frequency tunable liquid crystal Fabry-Perot etalon device that acts as a very narrow band-pass filter. This device has been developed primarily for wavelength multiplexing communication applications and consist of a crystal with partially mirrored surface on each end and transparent electrodes. When a voltage in the range of 3-5 volts is applied, the orientation of the molecules within the crystal change and allows to control the refractive index, as a result of this, this device can be used to conveniently control the pass-band of the Fabry-Perot filter. Liquid crystal Fabry-Perot interferometers can be used together with inexpensive broadband light sources to select the wavelength of interest.

A schematic diagram of the spectral interference microscope is shown in Fig. 2.7, the LC-FPI (liquid crystal fabry perot) works as tunable transmission element, a white light with a spectrum $sigma_m(\nu)$ is used as source, the LC-FPI transmit only a single line spectrum of the broadband source. The Michelson interferometer generates a signal:

$$g(x, y, \nu) = S(\sigma(\nu))(a(x, y) + b(x, y)\cos(2\pi l(x, y)\sigma(\nu))), \tag{2.15}$$

where $S[\sigma(\nu)]$ is the spectral intensity of the source light at the wavelength

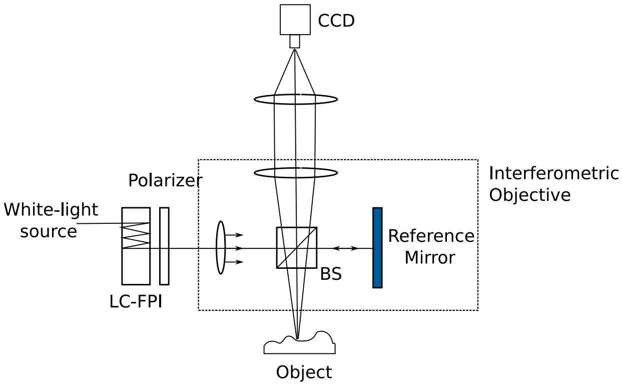

Figure 2.7: Spectral interference microscope.

$\sigma_m(\nu)$, $l(x,y)$ is the optical path difference between the object and the reference beam, which gives the information about the object height distribution. If the voltage applied to the LC-FPI vary in such way that the resonance wave number increases linearly with time $\sigma(t) = \sigma_m[\nu(t)] = \sigma_0 + \alpha t$, then the fringe pattern will vary sinusoidally with frequency proportional to the optical path difference:

$$g(x,y,t) = S(\sigma(t))(a(x,y) + b(x,y)\cos(2\pi\alpha l(x,y)t + 2\pi\sigma_0 l(x,y))) \,, \quad (2.16)$$

Thus the object height $h(x,y)$ can be determined from the optical path difference $l(x,y)$ when the temporal frequency $\alpha l(x,y)$ is measured from the fringe intensity variation at each pixel.

2.8 Coaxial Coimage Plane Projection and Observation Profilometry

Interferometry contouring methods enables the measurement of surface profiles without the problems of shading, but the optical setup are susceptible to vibrations, noise and air currents, which makes them unsuitable for industrial

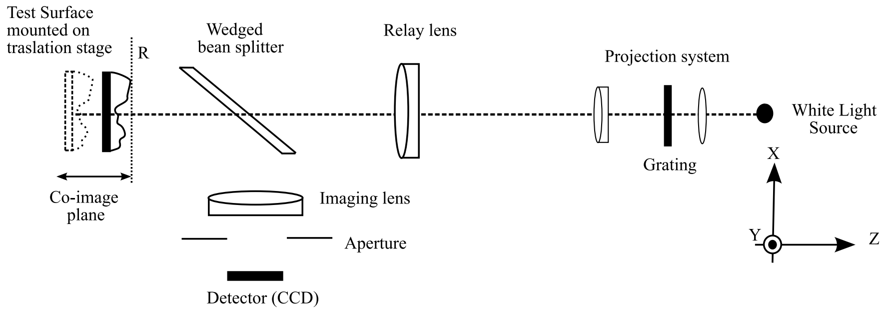

Figure 2.8: Optical arrangement for co-axial co-image plane projection and observation profilometry.

environments. Takeda[48] proposed an arrangement shown Fig. 2.8, this consist of a projection system that projects a grating pattern onto the conjugate image plane R, and a observation system that images plane R via a beam splitter onto the detector. Plane R is therefore a coimage plane for both the projection and observation systems that are arranged coaxially to eliminate shading problems. The contrast of the detected fringe pattern varies, because the object is moved using a translation stage, making that the peak of contrast occur where the scattering surface crosses the plane R. The surface height is therefore determined by detecting the translation required for maximum contrast at each pixel.

The use of projected grating patterns enables profiling of non-textured surfaces and the reduced depth of focus of the combined imaging system provides an improvement in the measured height resolution.

2.9 Laser Scanning

The most common techniques for 3D shape reconstruction in this area the scanning laser beam and scanning laser line technique. A sequence of equally space spots are projected over the object, the distance between spots will change according to the surface shape. These displacements of the light spots are obtained by calculating the maximum intensity and using the triangulation method, the information from this procedure allows the 3D shape reconstruction[49].

The scanner laser line technique uses a narrow line of light projected onto the object surface. In this procedure, the laser line will suffer deformations according to the surface topography, again by making use of the triangulation technique, the displacements of the laser line are calculated by the highest intensity position using peak detection method[50].

Muñoz A.[51] has proposed a method using laser light projection in which the displacement of the laser line is obtained by its skeleton which is determinate by calculating the maximum intensity over the x direction for a line that is vertically projected. This technique avoid the problems on fringe projection patterns such as the phase stepping procedure in order to calculate the phase.

2.10 Binary Coding of Projected Structured Light

Structured light projection is based on triangulation methods and use a projection system to illuminate the scene with a known light pattern coming from a known angle relative to the viewing angle Fig. 2.9. In locating a point $P(x, y, z)$ over the test surface, the camera pixel co-ordinates (x, y) determine two of three degrees of freedom and the projector is used to label the third. The surface height is obtained by labeling planes in space and this is achieved by projecting structured light patterns onto the test surface. The sections are labeled by the intensity of the illumination, the number of sections that can be labeled by a given projection in a single image is limited by the number of different intensities of light that can be generated. The dynamic range can be extended by a projection of temporal sequence of intensities for each light

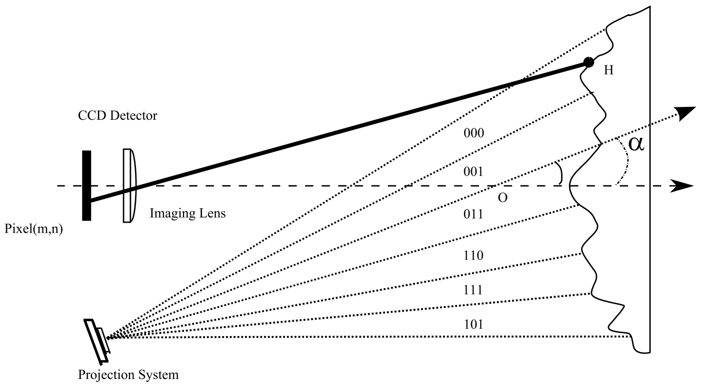

Figure 2.9: Optical arrangement for binary coding of projected structured light. Diagram shows one of a sequence of structured light patterns used in a 3-bit Gray code scheme to label the projection planes.

section, this sequences can be regarded as a code to identify a given section. In addition of the intensity values, the geometrical parameters are normally used in a calibration procedure to obtain the final 3D shape.

The choice of coding scheme influences the speed and resolution of the measurement, and optimum coding scheme should be self normalizing to simplify demodulation, identify each light section uniquely and only change one of the code digits between adjacent code-words to avoid decoding errors. The image analysis process can be regarded as a simple fringe codding method, in general this technique are only practical for incoherent fringe projection system and requires high stability of the optical set-up to maintain pixel registration during the measurement period.

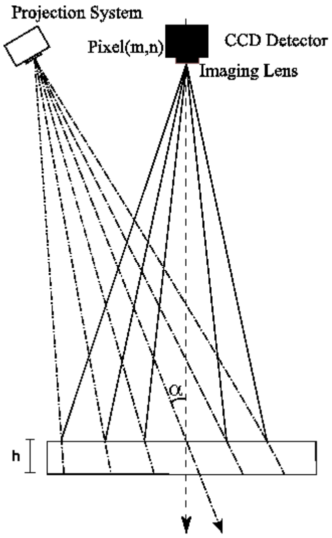

Figure 2.10: Optical arrangement for Optical arrangement for Moiré fringe projection.

2.11 Spatial Frequency Scanning of Projected Structured Light

Fringe projection consist in creating a family of plane parallel "‘sheets"’ of light in the volume surrounding the object under investigation[52]. Observation under an oblique angle gives an image where the fringe departure from straightness light is related to the shape of the object Fig. 2.10.

The structuring of the light in sheets can be obtained with a simple slide projector using an incoherent source. Interferometric techniques have the double advantage of creating directly a sinusoidal fringe pattern with infinite depth field. However, for large and deep field of view, one can no longer consider the light sheets as being parallel and plane. Corrections and calibrations must be made to take into account their real nature, as they constitute a family of hyperboloids.

The sensitivity of the technique is a function of the fringe spacing and the angle of observation. However, the main limitation is primarily the resolution of the imaging lens and camera used. Using state-of-the-art cameras and fringe analysis software, the depth resolution is on the order of one thousandth of the field of view. Projection Moiré is a way to increase the resolution of standard fringe projection. In particular, one can project on the object a very fine fringe pattern the image of which cannot be resolved directly by the detector. However, if this fringe pattern is resolved by the imaging lens of the camera, one can place a reference grating at the image plane. This grating creates a Moiré pattern with the fine line structure present on the objects image. The beat frequency is lower that the grating spatial frequency and can then be resolved by the detector.

2.11.1 Phase Shifting

Phase shifting technique constitute one of the two main families of fringe analysis. This technique is based on the possibility of obtaining multiple versions of a given interferogram. These images are acquired after modification of the phase of one of the two interfering waves. The result is a movement of the fringes in the image, without however changing the shape of the phase map. If fringes represent height contour plots, changing the phase difference of the waves by a constant quantity is equivalent to changing the origin of the contour lines. The contour lines are located differently but they still accurately describe the surface. These different versions of the interferogram lead to a mathematically correct extraction of the phase ϕ and permit the determination of the its sign.

With the capability to introduce controlled phase changes $\triangle\phi$ in a interferogram a sinusoidal profile changes to:

$$I(x,y) = I_0(x,y) + I_M(x,y)\cos(\phi(x,y) + \triangle\phi(x,y))\,, \tag{2.17}$$

the phase change or phase increment $\triangle\phi$ can vary across the interferogram, hence the possible dependence in (x, y). If $\triangle\phi$ is known, at least three equations are required to solve Equation (2.17) for the value of ϕ. A simple 3-image solution consist in recording images as follows:

$$\begin{aligned} I_1 &= I_0 + I_M \cos(\phi - \triangle\phi) \\ I_2 &= I_0 + I_M \cos(\phi) \\ I_3 &= I_0 + I_M \cos(\phi + \triangle\phi)\,, \end{aligned} \tag{2.18}$$

$$\phi = \arctan\left(\frac{1-\cos(\triangle\phi)}{\sin(\triangle\phi)}\frac{I_1 - I_3}{2I_2 - I_1 - I_3}\right)\,, \tag{2.19}$$

$$I_M = \frac{\sqrt{(1-\cos(\triangle\phi))^2(I_1 - I_3)^2 + (\sin(\triangle\phi))^2(2I_2 - I_1 - I_3)^2}}{2\sin(\triangle\phi)(1-\cos(\triangle\phi))}\,, \tag{2.20}$$

$$I_0 = \frac{I_1 + I_3 - 2\cos(\triangle\phi I_2)}{2(1-\cos(\triangle\phi))}\,, \tag{2.21}$$

when $\triangle\phi$ is equal to $\frac{2\pi}{3}$ Eqs (2.19), (2.20), (2.21) is simplified as:

$$\phi = \arctan\left(\sqrt{3}\frac{I_1 - I_3}{2I_2 - I_1 - I_3}\right)\,, \tag{2.22}$$

$$I_M = \frac{1}{3}\sqrt{3(I_1 - I_3)^2 + (2I_2 - I_1 - I_3)^2}\,, \tag{2.23}$$

$$I_0 = \frac{1}{3}(I_1 + I_2 + I_3)\,, \tag{2.24}$$

the phase is numerically obtained as an arctangent function. Taking into account the sign of both numerators and denominators, this yields a value in the range of $[0, 2\pi]$. The resulting modulo 2π image is often called a ”‘wrapped phase map”’. The simple 3-image algorithm presented can be generalized to N images.

2.12 Multiplexed Spatial Frequency of Projected Structures Light

Takeda[53] describes a technique based on projection structured light that requires only a single fringe pattern and permits phase unwrapping for discontinuous surfaces from a single acquired image. In this technique multiple phase maps with various phase sensitivities are spatial-frequency multiplexed into a single frame pattern to unambiguously determine the surface height. The acquired image is filtered by a two dimensional Fourier transform to demultiplex the spatial carrier frequencies, each being modulated in phase by the surface height with varying sensitivity.

Multiplexing spatial frequencies in the projected light pattern reduces fringe contrast and introduces difficulties during phase extraction. In particular, the filtering of the acquired image in the Fourier domain band-limits the broadband signal obtained for discontinuous surfaces, and therefore reduces the attainable signal to noise ratio compared to sequential projection and recording schemes.

2.13 Others Techniques

2.13.1 Digital Image Correlation

A recent method for 3D shape measurement had been proposed by Y.H. Huang[54], this method utilizes the magnification introduced by a non-telecentric lens and the local correlation of white light speckle patterns to estimate the 3D shape. The closer the object is to the camera, the larger it appears in the image plane. In this case, an in-plane translation was applied and the images before and after displacement differ by an amount equal to the in-plane displacement modulated by the difference in surface height.

The relations between the object and image coordinates in a simple imaging

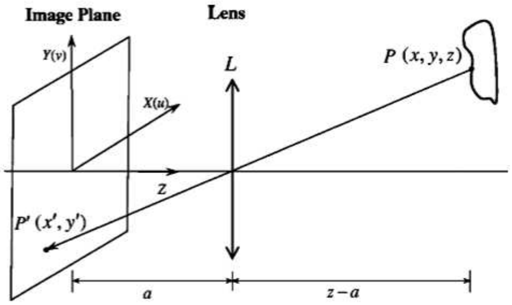

Figure 2.11: Optical setup for digital image correlation.

system can be expressed as:

$$\frac{x^{'}}{x} = -\frac{a}{z-a}\,, \tag{2.25}$$

and

$$\frac{y^{'}}{y} = -\frac{a}{z-a}\,, \tag{2.26}$$

where a represents the distance from the image plane to the lens, $(x^{'}$,$y^{'})$ the image coordinates, (x, y) the object coordinates, and z the distant between the object and the image plane. If the object is displaced by a translation Δx using the DIC to obtain $\Delta x^{'}$ the z coordinate can be obtained by:

$$z = a - \frac{\Delta x}{\Delta x^{'}}\,. \tag{2.27}$$

2.13.2 Shearing

An optical interferometric configuration sensitive to the first derivate of displacement is shown in Figure 2.12. The object D is illuminated by a inclined wave front at an angle θ and viewed through a Michelson interferometer[55, 56]. The Mirror M1 lies parallel to the plane X2 and M2 is inclined at a small angle α, to form two images of D overlapped in the plane I Fig. 2.13. The intensity at any point in the image will be the superposition of the light scattered

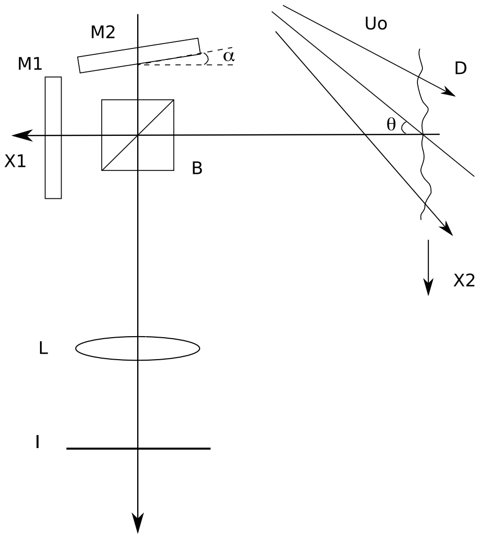

Figure 2.12: Optical setup of speckle pattern shearing interferometer.

from two adjacent points in the original object. The phase change of the light arriving at any point in the image I, will be given by:

$$\Delta\phi = \frac{2\pi}{\lambda}(d - d^{'})\,, \tag{2.28}$$

where d and $d^{'}$ are the respective displacements of two points in the object illuminating a single point in the image I. In the case of a normal illumination and assuming that the displacement of the two points illuminating a given point in the image plane will be sufficiently small, the phase change can be expressed as:

$$\Delta\phi = \frac{4\pi}{\lambda}\frac{\partial d_1}{\partial x2}S_2\,, \tag{2.29}$$

where S_2 represents the separation between the points that illuminate a point in the image, the sensitivity of the fringes can be varied by changing the relative orientation of M1 and M2.

The use of this interferometric optical setup, Fig. 2.12 leads to an easy way to measure slope of contour by shifting the light source between two

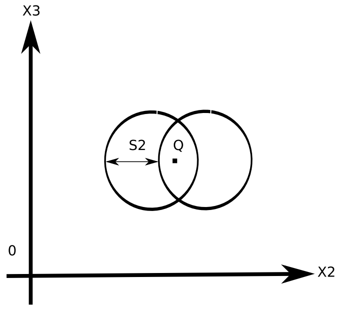

Figure 2.13: The sheared image geometry obtained using the arrangement shown in Fig. 2.12.

exposures[57], the quality of interferograms obtained is usually poor and the decorrelation effect strongly limits the performance of the method. In a similar method, the specimen was placed on a rotating platform and illuminated by an expanded laser beam, by recording two images before and after rotating the object, the resulting fringe pattern represents the object's surface directly[58].T. Santhanakrishnan[59] presents an improvement of the fringe contrast which can be achieved by using a two aperture mask placed in front of the camera lens with illumination over the optical axis. Other similar methods have introduced wavelength changes to obtain the same contouring effect[60].

Chapter 3

Temporal Phase Unwrapping

3.1 Phase Unwrapping

The optical techniques described in Chapter 2 have been developed to measure a wide range of physical parameters, with the advantage of non-contacting, and providing encoded information about physical parameters such as the 3D shape. These techniques require a numerical interpretation to be of optimal use to the scientist and engineers, the information recovered is usually encoded in the form of two dimensional (2-D) fringe patterns or interferograms. Any automatic quantitative evaluation of interferograms requires accurate phase measurement, independent from intensity fluctuations superimposed onto the interferograms. Two principal methods exist for extracting the underlying phase distribution from fringe pattern:

- Shifting the fringes through known phase increments.
- Fourier transform of a single pattern containing carrier fringes.

In both cases the calculated phase values are wrapped onto the range of $-\pi$ to π, and the process of phase unwrapping is the last difficult step. The goal of the phase unwrapping procedure is to remove the 2π phase discontinuities produced by the arctangent function. This process seems fairly obvious,

Fig. 3.1 shows how the discontinuities can be corrected by the following algorithm: we determine an offset phase distribution $\phi_o(x, y)$ that should be added to the discontinuous phase distribution $\phi_d(x, y)$ to transform it to a continuous distribution $\phi_c(x, y)$.

$$\phi_c(x, y) = \phi_d(x, y) + \phi_o(x, y)\,, \tag{3.1}$$

the first step in making this determination is to obtain the phase difference

$$\triangle\phi_d(x_i, y) = \phi_d(x_i, y) - \phi_d(x_{i-1}, y)\,, \tag{3.2}$$

between the ith sample point and the point preceding it, with the suffix i running from 1 to N to cover all the sample points. The fact that the sampling theorem demands at least two pixels per fringe and that the fringes usually cover several pixels therefore, the absolute value of the phase difference $\mid \triangle\phi_d(x_i, y) \mid$ is much less than 2π between two adjacent pixels. However it becomes almost 2π at points where the phase jumps occurs. The second step is to determine the offset value required to add in each sample point, starting from the point $x_0 = 0$. We set $\phi_0^x(x_i, y) = \phi_0^x(x_0, y)$ where $\phi_0^x(x_0, y) = 0$ for $i = 1, 2, 3, ..., k-1$ until the first phase jump is detected at the kth sample point. If the detection of the phase jump is positive, we set $\phi_0^x(x_k, y) = \phi_0^x(x_{k-1}, y) - 2\pi$, and if it is negative we set $\phi_0^x(x_k, y) = \phi_0^x(x_{k-1}, y) + 2\pi$. Again, we start to set $\phi_0^x(x_i, y) = \phi_0^x(x_k, y)$ for $i = k+1, i = k+2, i = m-1$, until the next phase jump occurs at the mth sample point, where the addition or subtraction of 2π is performed, with k now being replaced with m. Repeating this procedure of 2π phase addition or subtraction at the points of phase jumps, we can determine the offset phase distribution, as shown in Fig. 3.1(B), the addition of which to $\phi_d(x, y)$ gives a continuous phase distribution $\phi_c(x, y)$, as shown in Fig. 3.1(C).

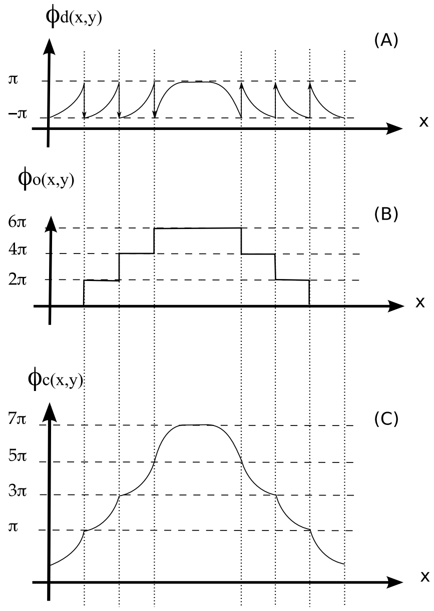

Figure 3.1: (A) Example of a phase distribution having discontinuities that are due to principal-value calculation; (B) offset phase distribution for correcting the discontinuities in (A); (C) continued profile of the phase distribution.

Phase unwrapping can in principle be carried out by any path, since the underlying phase distribution is a single valued function of position in the image, there are a lot of works with numerous solutions to process single wrapped phase images, however if the fringes are not sampled at a sufficiently high spatial frequency, the fringe pattern may be inherently discontinuous, or just the simple presence of noise can cause unwrapping errors that are reflected in a large 2π phase errors in regions of the image well away from the noise. For example an object containing holes or cracks, or consisting of several independent components, can have fringes truncated and isolated from other sets of fringes.

A wide variety of partial solutions to these problems has been suggested such as: Cellular automated methods[61] that use simple neighborhood rules applied sequentially to all pixels in the image with path independence that can be used in practical solutions. An alternative method based on identification of the discontinuity sources; cuts are then placed between sources of opposite sign[62], this method guarantees that the phase map is unique and independent of the path by which unwrapping take place. Bone has proposed a method in which the discontinuities sources are masked out with the application of a cellular automata method[2], the masked phase map could then have been unwrapped much faster even substituting the cellular automata method. The algorithms briefly described above, are known as ”spatial” algorithms in the sense that the phase map is unwrapped by comparing adjacent pixels or pixel regions within a single image. Once the unwrapping process in completed, the phase map has to be transformed into the corresponding physical quantity, displacement or shape. This is made by a calibration process in which sometimes it is necessary to make some hypotheses on the actual behavior of the object.

3.2 Temporal Phase Unwrapping

The basic idea behind the temporal phase unwrapping (TPU) is that the phase at each pixel is measured as a function of the time. Unwrapping is then carried out along the time axis for each pixel independently of the others, boundaries and regions with poor signal-to-noise ratios do not adversely influence good data points[63]. A set of four images creates a phase distribution $\phi_w(m, n, t)$ as shown in Fig. 3.2.

In practice the phase maps include boundaries and regions of high noise, in the TPU these regions form structures oriented along the time axis, provided the boundaries do not change with the time, and can therefore be avoided completely by unwrapping along paths parallel to the time axis. The wrapped phase change $\triangle\phi_w$ corresponding to the two instants t and (t-1), wrapped into the range (-π, π), can be calculated by using the following equations:

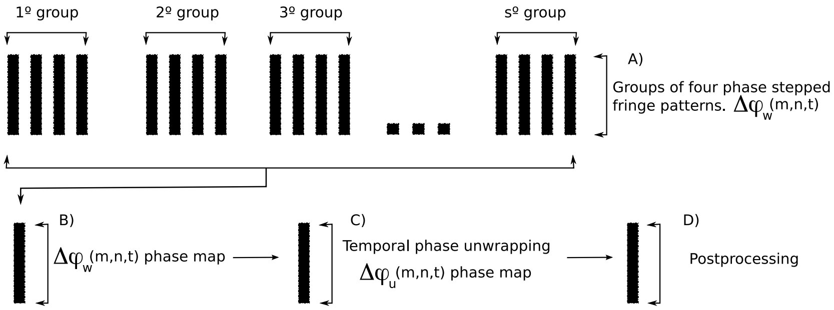

Figure 3.2: A group of fringe patterns stacks, each one with 4 phase stepped fringe patterns creating a wrapped phase map ϕ_w that is used in the TPU. The four main steps are illustrated within brackets: (A) Each group corresponds to a different pitch with phase-steeped fringe patterns, (B) Differences of consecutive phase maps, (C) Temporal phase unwrapping, (D) Postprocessing.

$$\triangle\phi_w(m,n,t) = \arctan\left(\frac{\triangle_{42}(t)\triangle_{13}(t-1) - \triangle_{13}(t)\triangle_{42}(t-1)}{\triangle_{13}(t)\triangle_{13}(t-1) - \triangle_{42}(t)\triangle_{42}(t-1)}\right), \tag{3.3}$$

$$\triangle_{ij}(t) = I_i(t) - I_j(t)\,, \tag{3.4}$$

a spatial smoothing operation can be carried out by convolving the numerator and denominator with a 3x3 kernel. Since phase maps include regions of high noise, if a spatial phase-unwrapping path crosses them, 2π phase errors can occur. In the temporal phase-map these forbidden regions form structures oriented along the time axis, provided the boundaries do not change with time. Therefore the spatial unwrapping errors could be completely avoided by unwrapping along paths parallel to the time axis. The number of 2π phase jumps between two successive measurements of the phase change can be found as:

$$d(m,n,t) = \frac{\triangle\phi(m,n,t)}{2\pi}\,, \tag{3.5}$$

and the total number of phase jumps is calculated through

$$v(m,n,s) = \sum_{t=1}^{s} d(m,n,t)\,, \tag{3.6}$$

finally, the unwrapped phase - difference map is obtained as

$$\triangle\phi_{unwrapped} = \triangle\phi_w(m,n,t) - 2\pi v(m,n,s). \tag{3.7}$$

3.3 Quality Map for Modulated Phase

When a series of phase shifted images are obtained, the four temporal algorithms are used to find the phase information. The following equations represent the intensities of the four shifted images[64].

$$I_0 = I_o + I_M \cos(\phi(x,y))\,, \tag{3.8}$$

$$I_1 = I_o + I_M \cos(\phi + \frac{\pi}{2}) = I_o + I_M \sin(\phi(x,y))\,, \tag{3.9}$$

$$I_2 = I_o + I_M \cos(\phi + \pi) = I_o - I_M \cos(\phi(x,y))\,, \tag{3.10}$$

$$I_3 = I_o + I_M \cos(\phi + \frac{3\pi}{2}) = I_o + I_M \sin(\phi(x,y))\,, \tag{3.11}$$

where I$_o$ is the average intensity, I$_M$ is the intensity modulation and ϕ is the unknown phase. Solving these equations for ϕ yields the following solution:

$$\phi(x,y) = \arctan\left(\frac{I_3 - I_1}{I_0 - I_2}\right)\,, \tag{3.12}$$

$$I_M(x,y) = \frac{\sqrt{(I_3 - I_1)^2 + (I_0 - I_2)^2}}{2}\,, \tag{3.13}$$

the phase value calculated through Equation (3.12) falls in the range ($-\pi$, π). The quantities in Eqs. (3.12) and (3.13) are estimators of the true phase and modulation respectively, and may differ from them due to random and systematic measurements errors. Data modulation is used to check quality of the data at each pixel. Therefore the data modulation, Equation (3.13), is used for generating the quality map for masking out pixels that produce noise. The quality map can be used to select pixels that give enough modulation for the proper functioning of the TPU, and to isolate pixels with low modulation. A mask, with 0 in the pixels of low modulation and 1 in the modulating pixels is obtained from histogram equalization and a threshold operation. As the equalization assumes equal probability for the modulation, a percentage of the equalized quality histogram is selected by choosing a threshold value. If the threshold is set too low, no enough pixels will be masked out; on the other hand, if the threshold is too high, it will cause too many pixels to be masked out, and isolated phase regions start to emerge. Defining the threshold value is hence a crucial point of the whole procedure, in our case we select a threshold value such as the pixels with 85% or more of modulation are selected. In the literature, other works try to solve the same problem considering boundaries and high noise regions[65, 62, 66].

Chapter 4

Experimental Results

4.1 Fringe Projection Setup

Recent developments on Spatial Light Modulator systems based on reflective liquid crystal microdisplays have allowed the technologies of Liquid Crystal over Semiconductors. In particular, the LCoS manufactured by Holoeye LC-R 2500 supports DVI-signals with XGA resolution (1024 x 768 pixels). The highest potential of the Spatial Light Modulators is that they have dynamic addressable diffractive elements that can be used for projection purposes. However, the projecting capabilities should be tailored for specific applications, and its performance should be assessed depending on the application.

In this work an LCoS is used to project fringe patterns over a 3D specimen using two different optical configurations. The first case is when the fringe projection patterns projected over the specimen, are formed by digital holograms. In this case, a routine coded in matlab generate holograms (kinoforms) that are displayed by the LCoS and the lens f = 30.5 cm, that is placed at the position labeled “Lens P1” with the object (LCoS) placed behind the lens inside of the focal distance range Fig. 4.1 . Therefore, the input object (LCoS) is placed at a distance d in front of the rear focal plane of the lens. The light incident on the input is a spherical wave converging towards the back focal

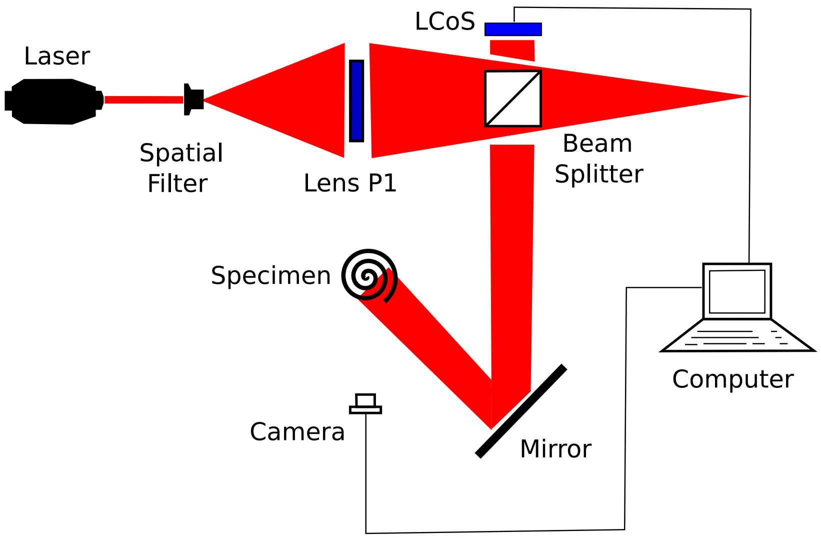

Figure 4.1: Optical setup: The fringe patterns are projected with a LCoS using kinoforms and a camera acquires the resulting images for further TPU data processing.

point of the lens. Assuming Fresnel diffraction the complex amplitude at the focal plane is given by[67]:

$$U_f(u,v) = \frac{A \exp^{j\frac{k}{2d}(u^2+v2)} f}{j\lambda d} \int_{-\infty}^{+\infty} \int_{-\infty}^{+\infty} t_a(\xi,\eta) P(\xi\frac{f}{d},\eta\frac{f}{d}) \exp^{-j\frac{2\pi}{\lambda d}(u\xi+v\eta)}\, d\xi\, d\eta\,, \tag{4.1}$$

where t_a is the complex amplitude of the input image, $P(\xi\frac{f}{d},\eta\frac{f}{d})$ is the pupil function, (u,v) are coordinates of the diffraction pattern, U_f is the amplitude and phase of the projected hologram, and (ξ,η) are the direction cosines. This has a magnification factor, namely the scale of the Fourier transform. This factor is under control of the experiment, by increasing d, the distance from the focal plane to the object, the size of the transform is made larger, by decreasing d the scale of the transform is made smaller. This let us to have different sizes of projection areas and hence different object sizes, experimental results gave us an approximately range between 7 mm to 30 cm.

The second consists of a fringe projection system Fig. 4.2 that is configured

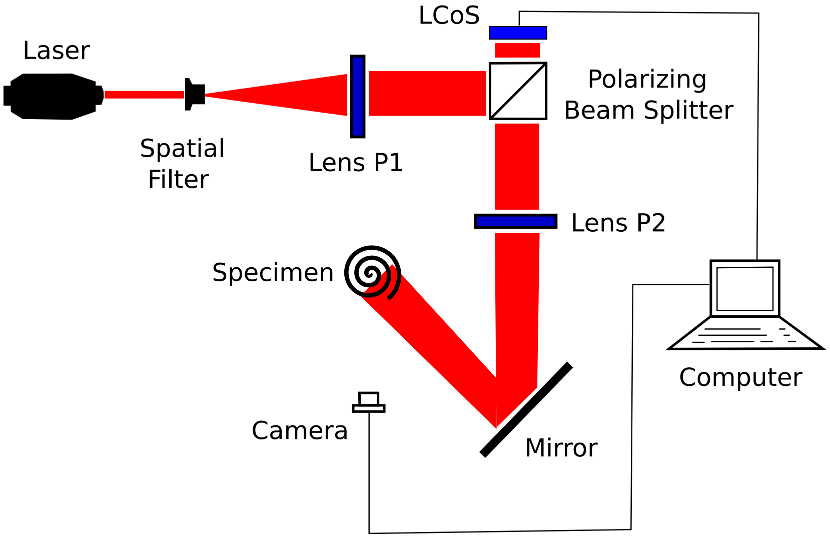

Figure 4.2: Optical setup: The fringe patterns are projected with a LCoS as a conventional computer projector and a camera acquires the resulting images for further TPU data processing.

as a conventional computer projector, to achieve this, a lens, $f = 30.5$ cm, is placed at the position labeled "Lens P2" to form an image of the fringe pattern that is sent to the LCoS for projecting over the specimen. The lens is located at 36.5 cm from the polarizing beam splitter, the LCoS is located at 1.5 cm from the polarizing beam splitter and it has been illuminated with collimate light using a lens, $f = 30$ cm, labeled "Lens P1". The mirror makes an angle between the specimen and the projection of 15^o. As the optical setup is a simple imaging system, the Gauss law for lenses let us know the exact position of the lens to project the fringe patterns over the specimen.

The fringe patterns were generated using a routine coded in Matlab environment and displayed trough a PC. We can use fringe pattern projection or holographic fringe projection (kinoforms), both with a size of 500x500 pixels with different fringe densities (each with four phase shifts); making use of the PC video output, the fringe patterns are transmitted to the LCoS and then projected over the specimen as shown in Figures 4.1 and 4.2.

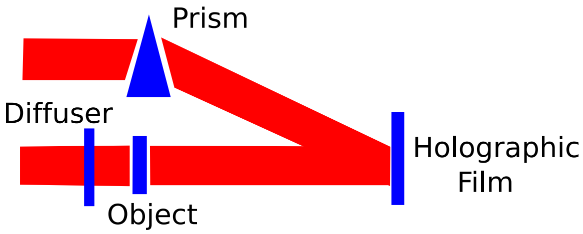

Figure 4.3: Optical setup: Method of introducing the reference bean, a prism is used to create the superposition of the two beams object and reference.

4.2 Projection Based on Computer Generated Holograms

A hologram records the field distribution that results from the light scattered by an object, since there is a one to one correspondence between the object and its scattered field, it is possible to record information about the object by mapping the scattered field, this mean that the Fresnel[68] or Fraunhofer diffraction pattern of the object is recorded and then used to produce an image of the original object. When the image of the object is reconstructed, there are flaws in the reconstruction as result of dust particles, vibrations and turbulence present in the optical system at the time in which the scattered light was recorded. A solution for these problems is the diffused illumination hologram[69]. The optical system in Fig. 4.3 shows a diffusing element placed between the source and the object, the light incident over the object now has a phase and amplitude which vary randomly from point to point, but in general terms this phase and amplitude relations are time invariant. This kind of illumination will produce a no recognizable Fresnel/Fraunhofer diffraction pattern or coarse structures in the reconstructed image; the most significant property of the diffused illumination holograms is that the imperfections in the optical elements will not degrade the quality in the reconstructed image.

In fact difussed illumination holograms are more immune to defects of the recording procedure than a conventional photography procedure. Now a days with the aid of computers the process of recording an hologram has changed, now it is possible to synthesize holograms, this task is motivated with the fact that the object is not physically present and its enough if the object is known in mathematical terms, computer generated holograms (CGH) make possible to study, by numerical simulations, certain holographic effects as mentioned above. The typical process of a CGH consist on four main steps, first the propagation of the complex amplitude from the object to the hologram plane, second is to encode the complex amplitude as a real non negative function (this is constrained by the gray scale on a image) and the final steps consist to transfer this information to a plotter device and to reduce it to a reasonable size for diffracting light. The principal limitation in CGH is the capacity of the computer for sampling the amplitude just in a finite number of points and the time required for the iteration procedure. One of the methods of fabricating a computer hologram can be done by recording the amplitude and phase of the scattered field [70, 71].

A new CGH is the kinoform[72, 73] which just have a single diffraction order and all the incident light is used to reconstruct the image in comparison with conventional CGH. The kinoform has computational advantages because neither the reference beam nor the image separation calculations are necessary. The kinoform is based on the idea that just the phase information of the scattered light is required for reconstructing the image of the object, the amplitude is assumed constant.

In an amplitude hologram the coded description of the object is due to the interference between the wavefront of the object W and the reference beam W_0, this give a transmittance function $T_a \propto I = \mid W + W_0 \mid^2$. In a phase hologram the complex transmittance is given by $T_p \propto e^{iI}$.

The process to create a kinoform involve a mathematical description of the object and the scattered light from it. Once the shape of the object is

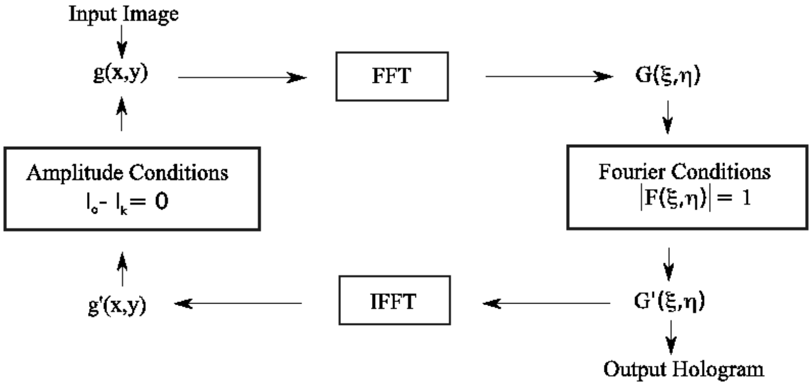

Figure 4.4: Schematic diagram to obtain a computer phase hologram.

determined, the distribution of its scattered field can be calculated by using computer algorithms. A common mathematical description of the object is a digital photography which gives the intensity distribution, the main point is to convert this intensity information onto phase information[74]. An easy example of this procedure can be obtained if we consider an object $f(x, y)$ which Fourier Transform can be expressed as:

$$F(\xi, \eta) = \mid F(\xi, \eta) \mid \exp^{i\phi(\xi,\eta)} , \tag{4.2}$$

therefore, the scattered light now is given by:

$$f(x, y) = \mid f(x, y) \mid \exp^{i\eta(x,y)} , \tag{4.3}$$

from Eqs. (4.2) and (4.3) we can observe that the most important factors are $\phi(\xi, \eta)$ and $\eta(x, y)$ since them contain the required information to obtain an hologram and the image coming from the hologram. In this work we used a phase hologram (kinoform) which is generated by an iterative Fast Fourier Transform (FFT) procedure [72].

There are several algorithms to obtain the phase in the kinoforms such as Detour - phase[75], phase retrieval[74], in - out approximation, and steepest -

descent, in this case the algorithm used was the error reduction because of its simplicity which is explained below.

As the kinoform is an object coded in phase, this condition works as a restriction that needs to be satisfied in the frequency domain, while the second restriction imposed by the space object is the intensity of the object used. In summary the conditions are:

- The image in the frequency space will only contain information of the phase.
- The absolute difference between the intensity of the original image and the image from the kinoform must be minimum.

When the conditions above are accomplished $G'(\xi, \eta)$ corresponds to the hologram, and after an iterative Inverse Fourier Transformation (IFFT) the image $g'(x.y)$ corresponds to the final reconstruction.

The Fig. 4.4 shows the procedure to obtain a phase hologram. The algorithm starts calculating the amplitude distributions of the object (image $g(x, y)$). Using the FFT we obtain a frequency distribution that is forced to accomplish the first condition above.

The new function that satisfies the first condition is again transformed using the IFFT, to obtain the intensity distribution. If the second restriction is satisfied, the frequency distribution in the Fourier space correspond to the kinoform, if not, a new image is generated as an input function with new phase distributions.

When the iterative process ends, the kinoform is expressed by Equation. (4.2), the phase representation is given in gray scale, this gray levels are quantified according with the phase changes in the range of $0 - 2\pi$.

4.3 Experimental Results with Projection Based on Computer Generated Holograms

The kinoforms were generated following the procedure described in Sect. 4.2 using as input the fringe patterns required by the TPU procedure.

Each corresponding hologram was generated by simulating a diffuser light source using a matrix of aleatory complex numbers. In general the amplitude of the wavefront scattered from the object is not constant but using a proper choice of the phase variations at the original object (equivalent to illumination using a diffuser) this amplitude is essentially constant. The phase of the complex number, was a random value less than a threshold in the interval $0 - 2\pi$ while its amplitude was given by the amplitude of the fringe pattern. The random phases were generated using the computer clock time as a seed, generating fringe patterns with random intensity variations. This was needed to smooth an input fringe pattern by averaging several projected fringe patterns previous to its use by the TPU algorithm described in Sect. 3.2.

The kinoforms were displayed in the computer monitor and projected onto the specimen under analysis by connecting the DVI monitor output to the LCoS as shown in Fig. 4.2. A Lumenera LU175M camera with a resolution of 1280 x 1024 pixels, interfaced to a PC was used to acquire the images in gray scale. The acquired images were used to generate the unwrapped phase maps, while a mask that blocks the phase noise and isolate pixels with bad modulation is generated from the quality map Sect. 3.3.

The reconstructed fringe pattern projected using the kinoform, has a granular texture that when acquired by the camera the speckle effect of the rough surface under test is added due to the use of coherent light. In order to reduce this granular texture, we averaged ten sets of the same fringe pattern but with different random noise projected over the object. These fringe patterns gave us also different speckle distributions as a result of the randomness given by the aleatory phase distributions; as a simple model we can consider $g(x, y)$ as the acquired image in the camera as:

$$g(x, y) = f(x, y) + n(x, y)\,, \tag{4.4}$$

where $n(x, y)$ is an additive noise, to reduce the noise the average of a set of images can be expressed by the expression:

$$\bar{g}(x, y) = \frac{1}{M}\sum_{i=1}^{M} g_i(x, y)\,, \tag{4.5}$$

we can note that by increasing M the intensity fluctuations around its mean value in each pixel comes down, and the function $\bar{g}(x, y)$ becomes $f(x, y)$. Assuming that the additional noise produces uncorrelated fringe patterns, it can be shown that the speckle contrast defined by:

$$c = \frac{[< \bar{g}^2 > - < \bar{g} >^2]}{< \bar{g} >}\,, \tag{4.6}$$

is reduced in accordance with the law

$$c = \frac{1}{\sqrt{M}}\,, \tag{4.7}$$

Experimental results were limited by the number of images M that our computing facilities allowed us. For $M = 10$ the projection and acquisition time was in the order of 15 min but the hologram generation time corresponding was of 36 hours. Given the large time needed for the tests, the noise reduction was also limited.

For the TPU a total of 35 averaged fringe patterns were processed, and ten fringe patterns were averaged for each pitch of the fringe patterns, as a result of this we found that the average was not enough to reduce the noisy signal produced by the speckle and simulated diffuser.

A second way to reduce the speckle noise is by integrating several speckles in each pixel camera, therefore we used an optical system with $f\sharp = 1.8$, the camera was placed at 50 cm from the object and the angle of fringe projection was of 10^o. An appropriate fringe density can be chosen using[76]:

$$S = \sqrt{\frac{L}{1.22\lambda}}, \tag{4.8}$$

where L is a measurement volume consisting of a cube of side L, λ is the wavelength of the laser; if L= 500 mm and $\lambda = 532nm$, thus the fringe density S is of 878. This density is too large for a quarter of the LCoS spatial resolution or 512x384 pixels. Therefore an optimum fringe density is necessary to suppress Moiré sampling effects, and to reduce the total time of the test, we found that for our setup our fringe density projection was optimum at 20 to 30 fringes in the field of view.

Once the setup geometry and the fringe density area were determined, the process of TPU is applied for getting the 3D shape reconstruction. 3D unwrapped phase usually have pixels with low modulation and residual noise, using the quality map describe in Sect. 3.3 we extracted a mask that was used to suppress the low quality phase values. This quality map is automatically generated previous to the TPU program, and then, a mask that leaves only the pixels with high values of modulation is obtained by enhancing the contrast through histogram equalization and threshold operation. For the object that we used the threshold value was selected as the 30% of the histogram values obtained after equalization.

Figure 4.5 shows the result obtained by projecting fringe patterns using kinoforms over a lens non specular surface, in this figure a calibration process[77, 78] was implemented to recover its original scale eliminating the spherical aberration. As we can observe the technique is able to recover the shape, but is not good enough to obtain resolutions less than a millimeter. This figure shows only some cracks over the surface object that are in the scale of a few millimeters, on the other hand smaller cracks can not be measured.

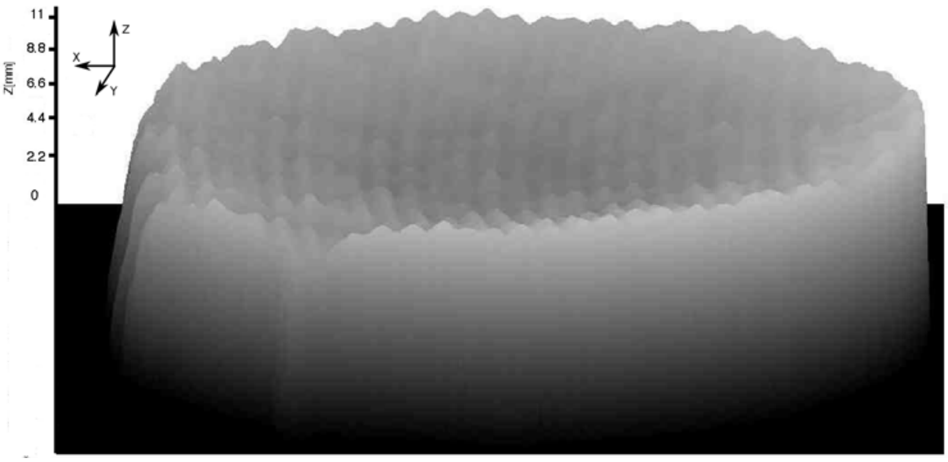

Figure 4.5: 3D shape reconstruction of a lens mold using kinoforms to project fringe pattern over a lens non specular surface (scale in millimeters).

4.4 Projection Based on Structured Light

The optical setup geometry used for fringe projection is shown in Fig. 4.6 which is the most popular configuration for the extraction of the 3D shape form, this task is an important procedure in industry in which it is desirable to transfer this information into a CAD program to yield a full 3D digital model for replicating purposes. The principle of phase measurement[79, 80, 81] has been a major researh topic in metrology area since the information of phase yields to the height data of the object.

Figure 4.6 shows a ray from the projector that interceps the object's surface at point Q', if the object were absent, the ray from the projector would intercept the reference plane R at point Q, this is visible by the camera as a displacement $\delta = \mid Q''Q \mid$ which is related with the fringe period as: $\delta = np$ where n is the fringe order and p is the period of the fringe pattern projected over the specimen, the relation between the displacement and the heigh can be expressed as[82]:

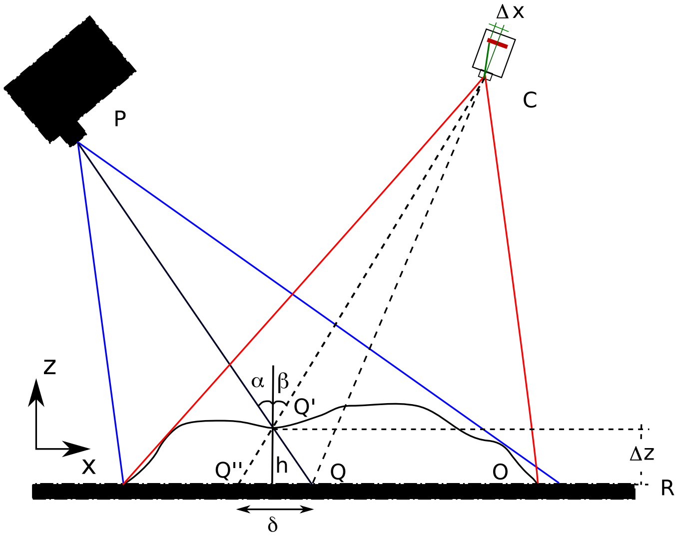

Figure 4.6: Geometry of structured light projection. P denotes projector, C denotes camera, R denotes reference plane.

$$\Delta Z = \frac{\delta}{tan(\alpha) + \tan(\beta)} \, , \tag{4.9}$$

A problem with Equation (4.9) is that angles α and β vary significantly over the field of view, even when $\beta = 0$ the variations of α must be accounted for. A second way to relate the displacement between the object and the reference plane in a height variation ΔZ is:

$$\Delta X = M \sin \alpha \Delta Z \, , \tag{4.10}$$

The value of ΔX represents the lateral offset of the fringe pattern recorded by the camera, Fig. 4.6, β is set to zero and M is the optical magnification. From Equation (4.10) it can be see that if M is too large, the sensitivity of the optical setup is high but the field of view becomes small. More over if α is large, the sensitivity also increases but this leads to shadowing problems.

The intrinsic way of projection causes the divergence of the fringe pattern, the angle of projection will produce a lateral variation of the fringes over the specimen, as consequence the fringes get wider due to angle of projection, and since the projector deliver the same light intensity over its projection (one light source), the image gets darker while at the opposite side the fringes are finer and brighter.

The oblique projection force to a calibration procedure to adjust the angle of projection and the dynamic range of the camera in order to adapt it to the brightness of the reflected light by the object under test; there are three principal sources of erros in the process of phase measurement. First, the nonuniformity distribution of the object surface reflectivity: if the reflectivity changes fast along the surface, the error becomes large. Second, the contrast in the fringe pattern: if the projected fringes have a high contrast the error becomes small. Third, the sinusoidal intensity variations across space and time: the projected fringes are in fact a discrete version of a sine signal, the number of gray levels used in the projection will restrict the sample rate.

The relation between spatial changes ΔX and the detected phase $\Delta\phi$ is given by Equation (4.11) were T is the average fringe period, it can be seen that if T gets smaller, then changes in $\Delta\phi$ gets larger increasing the sensitivity of the system. The fringe period is an important factor, as it gets finer the sensitivity increases until a limit is reached in which the contrast drops down all together with pixel modulation increasing therefore the error rate.

$$\Delta\phi = \frac{2\pi\Delta X}{T}, \tag{4.11}$$

An appropriate fringe density can be chosen using Equation (4.8) as reported by Huntley[62].

4.5 Experimental Results with Structured Light

When voltage is applied to the LCoS elements, it produces phase changes to the reflected light that are transformed in amplitude modulation by the polarizing beam splitter of Fig. 4.2. However, the LCoS can be operated as a phase-only modulator and many techniques for calibrating the liquid crystal have been proposed for phase and amplitude modulation [83, 84, 85, 86, 87].

In order to obtain an optimum optical configuration for amplitude or phase modulation, a desirable physical model for the liquid crystal(LCD) is necessary to predict the amplitude and phase modulation. In the literature we can find many works describing models of the LCD by using Jones matrix theory[88, 89, 90, 91, 92], the use of Jones matrix has many advantages, it is a complex matrix of size 2x2 and each element is proportional to the electric field, the disadvantages are that it is restricted to monochromatic and polarized light and the use of complex magnitudes which in some case leads to the use of complex mathematical expressions.

In this work the LCoS was configured to produce amplitude-only modulation, and its calibration procedure is explained in Appendix A. A gray scale fringe pattern has been created with a personal computer (PC) and then projected onto the object surface by using the LCoS projection system. The acquired images were grabbed with a camera, these images are used to generate the unwrapped phase map following the procedure described in Sect. 3.2, while a mask is generated from the quality map, Sect. 3.3, in order to eliminate noise and to isolate pixels with bad modulation.

The projector used in this experiment Holoeye LC-R 2500 supports DVI-signals with XGA resolution (1024 x 768 pixels); the camera used was Lumenera LU175M with a resolution of 1280 x 1024 pixels and automatic control light gain. The fringe patterns were generated using a routine coded in Matlab environment, making use of the PC video output the fringe patterns are transmitted to the LCoS and then projected over the specimen Fig. 4.1.

In order to obtain an optimum fringe density, suppress noise, Moire or sampling effects and the effect of diverging light illumination in the area of analysis, the spatial locations of projector, camera and object must be adjusted to obtain a good quality map in the 3D shape reconstruction, referring to the scheme in Fig. 4.2, if the distance between the LCoS and lens P2 is equal to 38 cm, the angle of projection $\alpha = 15^o$, $f\# = 2.5$ and depth focus of 2 cm, the upper limit of the fringe projection pattern can be set to 40 fringes in an area of projection of 3x3 cm.

Once setup geometry and fringe density are assessed, the process of TPU is applied for extracting 3D shape. Low reflection on the object usually generates pixels with bad modulation and noise. Using the quality map describe in Sect. 3.3 we extracted a mask that was used to suppress the low quality phase values. This quality map is automatically generated in the TPU program, and then, the mask is obtained enhancing the contrast through histogram equalization and threshold operation. In particular, all quality values below the defined threshold are set to zero, while values beyond the threshold will set to one. If the threshold is set too low, no enough pixels will be masked out; on the other hand, if the threshold is too high, too many pixels will be masked out, and isolated regions will appear. Hence, defining the threshold value is a crucial point of the whole procedure. For the specimens that we used the threshold value was selected between the 3% and 85% of the histogram values obtained after equalization. The threshold value has a very high dependence with the reflectance of the object under analysis.

Finally a low pass spatial filter is applied for the 3D shape reconstruction to suppress residual noise. However, the size used can affect the final masking process. The final 3D reconstruction of the TPU using linear pitch increments for objects under test are shown in Fig. 4.7 to Fig. 4.9.

The calculation of the shape from phase data, (Φ, m, n) to (x, y, z), its in principle a simple calibration process, but in practice is complicated by the number of degrees of freedom involved in the optical setup, camera, projector position and distortion introduced by the objective lenses. The calibration consist in two steps: convert $\Phi(m, n)$ to $z(m, n)$ and convert (m, n, z) to (x, y, z),

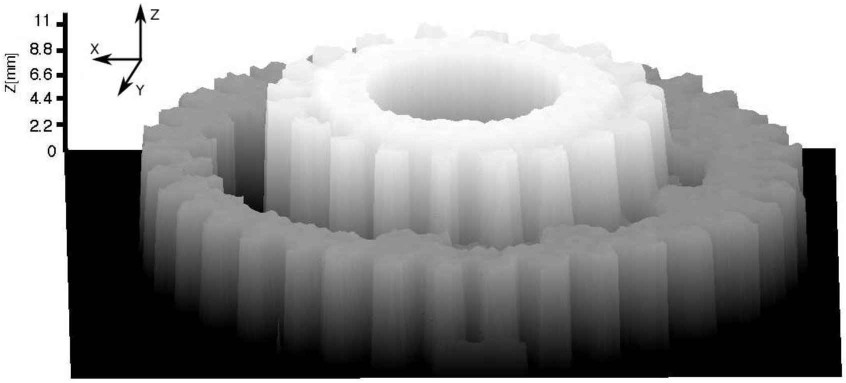

Figure 4.7: 3D shape reconstruction of a gear using fringe patterns with structured light (scale in millimeters)..

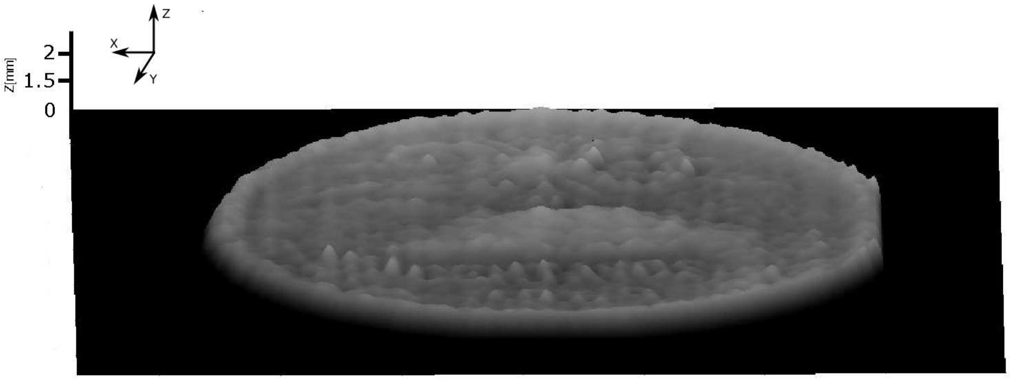

Figure 4.8: 3D shape reconstruction of a coin using fringe patterns with structured light (scale in millimeters)..

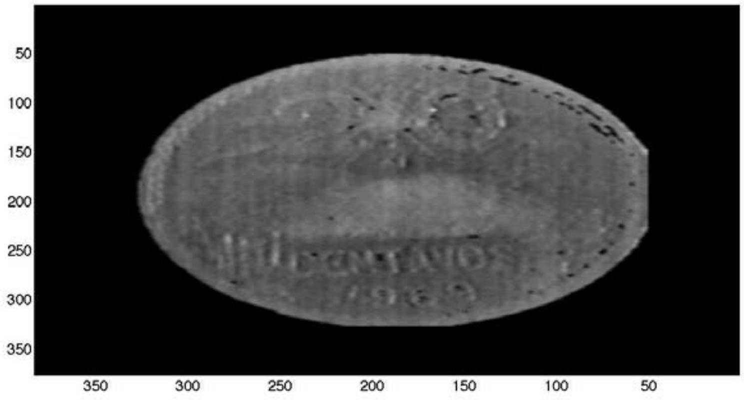

Figure 4.9: 3D shape reconstruction of a coin using fringe patterns with structured light (scale in pixels).

this procedure is described in Appendix B.

After the system was calibrated, it was tested by measuring a reference plane, Fig. 4.10 shows a cross section of a typical result, as we can observe the measured phase transformed to z values in millimeters has high frequency changes due to the no constant behavior in the amplitude modulation and systematic errors as described by J. Campos[92]. The problem in the amplitude modulation and even more in phase modulation is caused by a certain amount of depolarization in the LCoS reflected beam, this problem has a dependence on the addressed gray level and on the incident state of polarization. Basically as the input to the LCD is a video signal, there is a low frequency in the vertical direction, and a high frequency in the horizontal video signal. When the frequency is very high along the horizontal direction, the signal is limited in band by the electronic circuit reducing the modulation capacity of the LCoS.

The standard deviation of the surface profile is calculated as $44.8\mu m$. Figure 4.11 shows an unwrapped phase map of a plastic gear as a test object, this result would not be possible by the conventional spatial method. The object was prepared for the experiment being cleaned and coated with a thin layer of

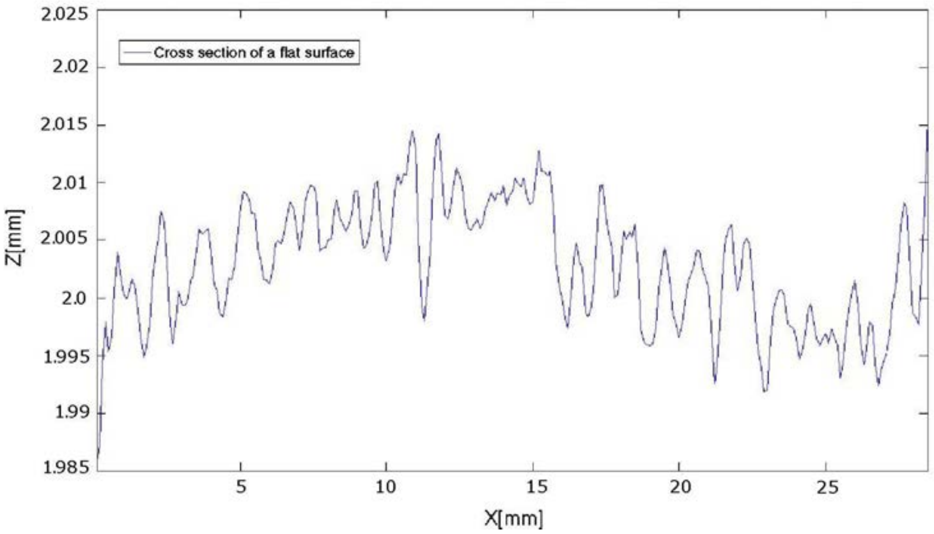

Figure 4.10: Cross section of a 3D shape reconstruction of a flat reference surface (positioned at z = 2mm).

white paint. Missing points on the surface belong to low modulation regions, shadows or problems with the reflectivity of the test objects.

Figure 4.8 and Figure 4.9 show the result of the TPU when is applied to a coin which surface is not clean or prepared for the experiment as was the gear. In this case we can observe that the signal to noise ratio is poor and hence a notorious change in the reflectivity of the object which is outside of the parameters in the intensity calibration. It can be seen that an increment in the wrapped maps used in the TPU will improve the final result as shown in Figure 4.12 left, the TPU is a kind of average procedure. It is important to realize that the number of fringes projected over the specimen are not independent variables in the TPU since the values of $\Delta\phi(t)$ depend each other. For example, $\Delta\phi(t) = \phi(t) - \phi(t-1)$ and $\Delta\phi(t+1) = \phi(t+1) - \phi(t)$ so that $\Delta\phi(t)+\Delta\phi(t+1) = \phi(t+1)-\phi(t-1)$ and errors in measuring $\phi(t)$ automatically cancel out, this mean that errors in the intermediate phase values $\phi(m, n, 1)$ and $\phi(m, n, s-1)$are automatically canceled, only errors in the initial and final map contribute to the measured phase change.

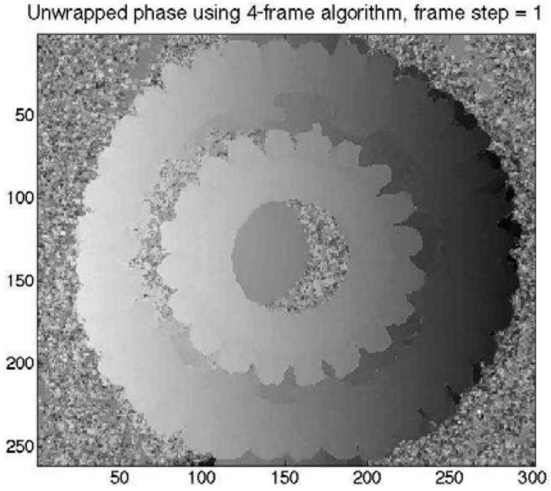

Figure 4.11: Unwrapped phase map showing a gear with 4 phase stepping algorithm.

In summary, the results obtained gave us a resolution below of the range of millimeters, and a shape in which we can distinguish the different parts of the gear and even of the coin. In order to obtain a better assessment of the resolution obtained by using this technique, we tested the shape of different metal gauges placed next to each other. The experimental results presented in Appendix B show us a resolution in the range of 0.64 μm, showing an improvement the results obtained by the holographic projection setup.

Nowadays it is possible to find in the literature research focused in the use of the TPU algorithm achieving higher improvements and hence better accuracy in the phase measurement procedure[93, 94]. Many companies actually are working for creating devices that can extract the 3D shape from different areas such: as medical engineering, reverse engineering, measuring works of art and mold making. Companies like 3DShape[95] report resolution in the range of 130 μm to 5 nm, Phase vision[96] 50 μm in a volume of 1x1x1 mm and Creaform3d[97] with a resolution of 0.1 mm.

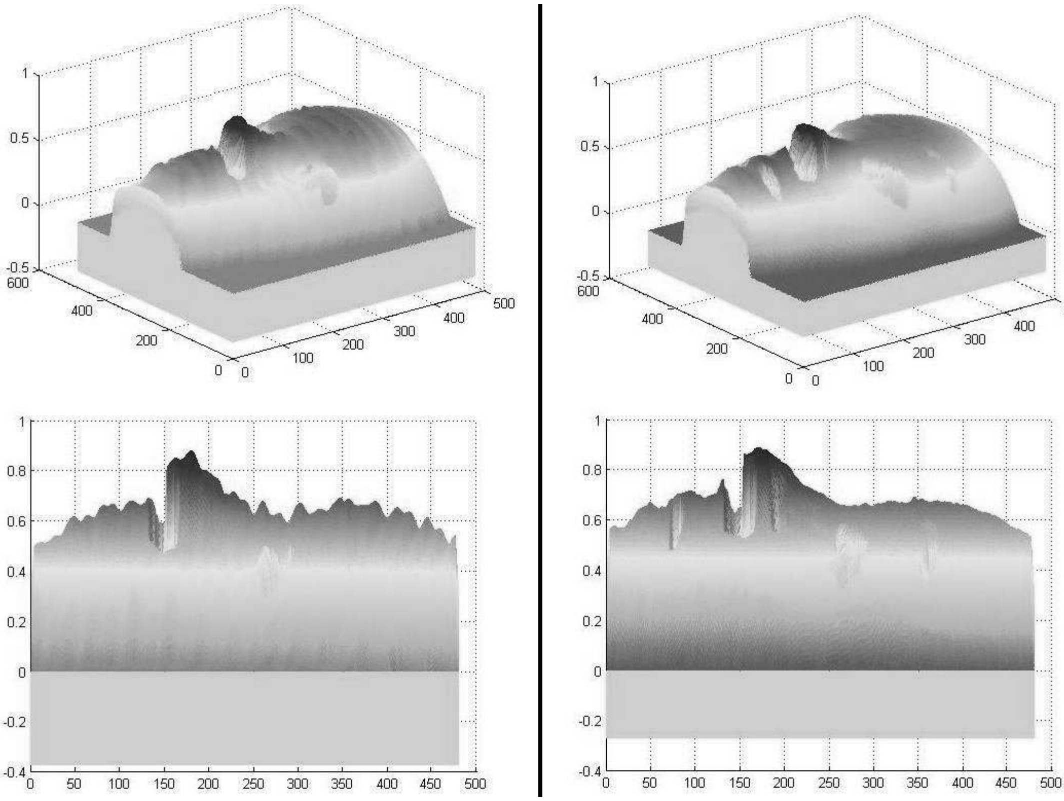

Figure 4.12: 3D shape reconstruction of a face obtained by TPU algorithm using a multimedia projector based on DLP technology: left 4, right 10 incremental maps (normalized scale).

Chapter 5

Conclusions

This work reports the utilization of an LCoS for 3D shape reconstruction using the TPU. A quality mask approach allows to extract valid information of the 3D shape.

The investigated holographic technique for the measurement of surfaces shape, allowed us to analyze different areas without making any important changes to the optical setup, giving us the opportunity to measure objects with areas in the range of $30 - 1$ cm . The main drawback of this technique is found in the noise average procedure, the computational time required to obtain the set of images used in this work was too long, over 36 hours for one PC; and the number of images was not enough to reduce the noise to an acceptable level. The technique structured light projection, produced much better results that the holographic technique, obtaining a resolution of approximately 0.064 millimeters. This resolution can be improved using a projector and camera with a higher dynamic range of gray levels and resolution, this will allow us to increase the sample range in the projected fringe pattern, and to detect with a better accuracy the intensity levels of the fringes over the specimen.

The main contributions of this work are: the exploration of the LCoS technologies as an element for projection of fringes adapted for the TPU algorithm, the demonstration of the superior performance of the LCoS amplitude projection scheme, compared to the holographic projection in the TPU applications, and the introduction of quality mask in the TPU algorithm to mask out common errors.

Problems in the behavior of the LCoS used in this work were also identified. The Holoeye LC-R 2500, showed experimentally a degree of depolarization in the reflected light, that lead us to solve problems in the amplitude and phase modulation, limiting the range of work to a certain numbers of specific gray levels.

The immediate future work is to obtain a physical model for the liquid crystal(LCD) that can predict the amplitude and phase modulation, this will make possible an improvement in the deep resolution of the system and even more this can allow the application of the holographic technique with improving results that can offer new technological applications in the areas of medical holography, optical image processing, and holographic microfiche.

Bibliography

[1] J. M. Huntley, "Three-dimensional noise-immune phase unwrapping algorithm," *Appl. Opt.* **40**, pp. 3901–3908, 2001.

[2] D. J. Bone, "Fourier fringe analysis: the two-dimensional phase unwrapping problem," *Appl. Opt.* **30**, pp. 3627–3632, 1991.

[3] H. Lim, W. Xu, and X. Huang, "Two new practical methods for phase unwrapping," in *Proceedings of the 1995 International Geoscience and Remote Sensing Symposium*, IEEE., ed., *IGARSS '95. Quantitative Remote Sensing for Science and Applications* **1**, pp. 196–198, 1995.

[4] W. Xu and I. Cumming, "A region growing algorithm for in-sar phase unwrapping," in *Proceedings of the 1996 International Geoscience and Remote Sensing Symposium*, IEEE, ed., *GARSS '96. Remote Sensing for a Sustainable Future* **4**, pp. 2044–2046, 1996.

[5] J. A. Quiroga, A. Gonzalez-Cano, and E. Bernabeu, "Phase unwrapping algorithm based on an adaptive criterion," *Appl. Opt.* **34**, pp. 2560–2563, 1995.

[6] T. Instrument, "Dlp," November 2007. `http://www.dlp.com`.

[7] JVC, "Drawbacks of lcd and dlp," November 2007. `http://www.jvc.com/presentations/hdila/drawbacks.html`.

[8] SONY, "Sxrd," November 2007. `http://www.sony.net/SonyInfo/News/Press_Archive/200302/03-008E/`.

[9] B. CO., "Gen ii lcos," November 2007. `http://www.holoeye.com/lcos_microdisplays_specs.html`.

[10] J. Consumer, "D ila," November 2007. `http://tv.jvc.com/`.

[11] H. K. Liu, J. A. Davis, and R. A. Lilly, "Optical data processing properties of a liquid crystal television spatial light modulator," *Opt. Lett* **10**, pp. 635 – 637, 1985.

[12] H. K. Liu and T. H. Chao, "Liquid crystal television spatial light modulators," *Appl. Opt.* **28**, pp. 4772 – 4780, 1989.

[13] J. A. Davis, D. M. Cottrel, J. Campos, M. J. Yzuel, and I. Moreno, "Encoding amplitude information onto phase only filters," *Appl. Opt.* **38**, pp. 5004 – 5013, 1999.

[14] G. D. Love, "Wavefront correction and production of zernike modes with a liquid crystal slm," *Appl. Opt.* **36**, pp. 1517 – 1524, 1997.

[15] J. Gourlay, G. D. Love, P. M. Birch, R. M. Sharples, and A. Purvis, "A real time closed -loop liquid crystal adaptive optics system: first result," *Opt. Commun* **137**, pp. 17 – 21, 1997.

[16] A. Tanone, Z. Chang, C.-M. Uang, F. T. S. Yu, and D. A. Gregory, "Phase modulation depth for a real time kinoform using a liquid crystal television," *Opt. Eng* **35**, pp. 517 – 521, 1993.

[17] Jian-Yu, K.-Y. Wu, and S.-I. Wong, "Spatial light modulator constructed from ferroelectric liquid crystal with twisted structure," *United Stated Patent* **6141076**, pp. 1 – 19, 2000.

[18] J. S. Patel and R. Bank, “Twisted ferroelectric liquid crystal modulator for providing gray scale,” *United Stated Patent* **5172257**, pp. 1 – 9, 1991.

[19] Jian-Yu, K.-Y. Wu, and S.-I. Wong, “Spatial light modulator employing voltage gradient pixels, and associate methods,” *United Stated Patent* **7268849**, pp. 1 – 10, 2007.

[20] JVC, “Jvc extends its lineup of proprietary d-ila high-resolution reflective liquid crystal devices with three devices including 0.8-inch full hd spec version,” November 2003. `http://www.jvcdig.com/news`.

[21] N. Collings, J. Gourlay, D. G. Vass, H. J. White, C. Stance, and G. M. Proudley, “Measurement on ferroelectric liquid crystal spatial light modulators contrast ratio and speed,” *Appl. Opt.* **34**, pp. 5928 – 5931, 1995.

[22] D. J. McKnight, K. M. Johnson, and R. A. Seratti, “256x256 liquid crystal on silicon spatial light modulator,” *Appl. Opt.* **34**, pp. 5928 – 5931, 1995.

[23] JVC, “D-ila,” November 2007. `http://www.jvcdig.com/`.

[24] J. D. Corless, M. Greenberg, and S. C. Olson, “A taxonomy of optical architectures for lcos projection displays,” in *Nonimaging Optics and Efficient Illumination Systems*, R. Winston and R. J. Koshel, eds., *Proc. SPIE* **5529**, 2004.

[25] S. Arnold, E. Gardner, D. Hansen, and R. Perkins, “An improved polarizing beamsplitter lcos projection display based on wire grid polarizers,” *SID 01 DIGEST* **52**, pp. 1282 – 1284, 2001.

[26] F. Chen, G. M. Brown, and M. Song, “Overview of three-dimensional shape measurement using optical methods,” *Opt. Eng.* **39**, pp. 10–22, 2000.

[27] A. P. Witkin, "Recovering surface shape and orientation from texture," *Artificial Intelligence* **17**, pp. 17–45, 1981.

[28] D. Marr and T. Poggio, "A computational theory of human stereo vision," in *Proceedings of the Royal Society of London*, JSTOR., ed., *Series B, Biological Sciences* **204**, pp. 301–328, 1979.

[29] Kriegman, D. Triendl, E. Binford, and T.O., "Stereo vision and navigation in buildings for mobile robots," in *IEEE Transactions on Robotics and Automation*, IEEE., ed., *Robotics and Automation* **5**, pp. 792–803, 1989.

[30] R. T. Framkot and R. Chellappa, "A method for enforcing integrability in shape from shading algorithms," *IEEE pattern analysis and machine intelligence* **10**, pp. 439–451, 1988.

[31] C. vision and pattern recognition IEEE, eds., *A simple algorithm for shape from shading*, (92), IEEE, 1992.

[32] H. Hayakawa, "Photometric stereo under a light source with arbitrary motion," *JOSA A.* **11**, pp. 3079–3099, 1994.

[33] K. M. Lee and C. C. J. Kuo, "Surface reconstruction from photometric stereo images," *JOSA A.* **10**, pp. 855–868, 1993.

[34] A. Archive, November 2007. `http://www.univie.ac.at/Luftbildarchiv/wgv/intro.htm`.

[35] T. basics of Photogrammetry, November 2007. `http://www.geodetic.com/Whatis.htm`.

[36] ISPRS, ed., *Weighted geometric objects constraints integrated in a line photogrammetric bundle adjustment*, (XXXIII), 2000.

[37] R. K. Erf, *Speckle Metrology*, Academic Press Inc., 1978.

[38] C. Joenathan, B. Pfister, and H. J. Tiziani, "Countouring by electronic speckle pattern interferometry employing dual beam illumination," *Appl. Opt.* **29**, pp. 1905–1911, 1990.

[39] D. D. Aguayo, "Detección de forma y deformaciones por espi," *Tesis de Maestría* **CIO**, 2004.

[40] R. R. Vera, "Optical gauging of diffuse surfaces by electronic contouring," *Optics and Lasers in Engineering* **26**, pp. 101–114, 1997.

[41] R. R. Vera, D. Kerr, and F. M. Santoyo, "Electronic speckle contouring," *JOSA A* **9**, pp. 2000–2008, 1992.

[42] D. Paoletti and G. S. Spagnolo, "Fast fourier transform electronic speckle contouring for diffuse surfaces profilometry," *Optics and Laser in Engineering* **20**, pp. 87–96, 1994.

[43] M. Wong-Tamez, A. Martínez, J. A. Rayas, D. I. S. García, and A. Serrano-Heredia, "Contorneo de superficie por espi utilizando un sistema fuera de plano implementado con fibras ópticas," *III Taller de Procesamiento de Imagenes y Óptica* **CIMAT**, 2006.

[44] M. Takeda and H. Yamamoto, "Fourier transform speckle profilometry: three dimensional shape measurements of diffuse objects with large height steps and/or spatially isolated surfaces," *Appl. Opt.* **33**, pp. 7829–7837, 1994.

[45] M. Takeda, H. Ina, and S. Kobayashi, "Fourier transform method of fringe-pattern analysis for computer-based topography and interferometry," *JOSA A.* **72**, pp. 156–160, 1982.

[46] T. Kreis, "Digital holographic interference-phase measurement using the fourier-transform method," *JOSA A.* **3**, pp. 847–855, 1986.

[47] M. Kinoshita, M. Takeda, H. Yago, Y. Watanabe, and T. Kurokawa, "Optical frequency domain imaging microprofilometry with a frequency tunable liquid crystal fabry perot etalon device," *Appl. Opt.* **38**, pp. 7063–7068, 1999.

[48] M. Takeda, T. Aoki, Y. Miyamato, H. Yago, Y. Watanabe, and T. Kurokawa, "Absolute three dimensional shape measurement using coaxial and coimage plane optical system and fourier fringe analysis for focus detection," *Optical Engineering.* **39**, pp. 61–68, 2000.

[49] L. Zeng, H. Matsumoto, and K. Kawachi, "Simultaneous measurement of the position and shape of a fringe pattern projection method with laser scanning technique," *Opt. Eng.* **37**, pp. 1500–1504, 1998.

[50] W. C. Tai and M. Chang, "Noncontact profilometric measurement of large form parts," *Opt. Eng.* **35**, pp. 2730–2735, 1996.

[51] J. A. M. Rodriguez, R. R. Vera, and M. Servin, "Direct object shape detection based on skeleton extracting of a light line," *Opt. Eng.* **39**, pp. 2463–2471, 2000.

[52] R. E. Brooks and L. O. Heflinger, "Moire gauging using optical interference patterns," *Appl. Opt.* **8**, pp. 935–940, 1969.

[53] M. Takeda, G. Quan, M. Kinoshita, H. Takai, and Y. Takahashi, "Frequency multiplexe fourier transform profilometry: a single shot three dimensional shape measurement of objects with large height discontinuities and/or surface isolations," *Appl. Opt.* **36**, pp. 5347–5354, 1997.

[54] Y. H. Huang, C. Quan, C. J. Tay, and L. J. Chen, "Shape measurement by the use of digital image correlation," *Opt. Eng.* **44**, pp. 0870111–0870117, 2005.

[55] R. Jones and C. Wykes, *Holographic and speckle interferometry A discussion of the theory practice and application of the techniques*, Cambridge, 1983.

[56] R. M. Groves, S. A. James, and R. P. Tatam, “Shape and slope measurement by source displacement in shearography,” *Optics and Lasers in Engineering* **41**, pp. 621–634, 2004.

[57] C. Tay, H. Shang, A. Poo, and M. Lou, “Measurement of surface coordinates and slopes by sherography,” *Optic and Laser Technology* **24**, pp. 209–213, 1992.

[58] Y. He, C. Tay, and H. Shang, “Digital phase-shifting shearography for slope measurement,” *Opt. Eng.* **39**, pp. 1586–1590, 1999.

[59] T. Santhanakrishanan, P. K. Palanisamy, N. K. Mohan, and R. S. Sirohi, “A new optical configuration in speckle interferometry for contouring of three dimensional objects,” *Opt. Commun.* **152**, pp. 19–22, 1998.

[60] W. Steinchen and L. Yang, *Digital Sherography Theory and Application of Digital Speckle Pattern Shearing Interferometry*, SPIE Press, 2003.

[61] D. C. Ghiglia, G. A. Mastin, and L. A. Romero, “Cellular automata method for phase unwrapping,” *JOSA A* **4**, pp. 267–280, 1987.

[62] J. M. Huntley, “Noise-immune phase unwrapping algorithm,” *Appl. Opt.* **28**, pp. 3268–3270, 1989.

[63] J. M. Huntley and H. Saldner, “Temporal phase-unwrapping algorithm for automated interferogram analysis,” *Appl. Opt.* **32**, pp. 3047–3052, 1993.

[64] J. M. Huntley, *Automated analysis of speckle interferograms, Chap. 2*, Wiley, 2001.

[65] A. Asundi and Z. Wensen, “Fast phase-unwrapping algorithm based on a gray-scale mask and flood fill,” *Appl. Opt* **37**, pp. 57–66, 1998.

[66] M. A. Herraez, D. R. Burton, M. J. Lalor, and M. A. Gdeisat, “Fast two-dimensional phase-unwrapping algorithm based on sorting by reliability following a noncontinuous path,” *Appl. Opt* **41**, pp. 7437–74444, 2002.

[67] J. W. Goodman, *Introduction to Fourier Optics*, The McGraw - Hill Companies, Inc., Stanford University, 1988.

[68] J. L. J. Perez, A. O. Perez, and L. R. B. Valdos, “Nonredundant calculations for creating fresnel holograms,” *Appl. Opt.* **36**, pp. 7437 – 7443, 1997.

[69] E. N. Leith and J. Upatnieks, “Wavefront reconstruction with diffused illumination and three dimensional objects,” *JOSA A* **54**, pp. 1295 – 1301, 1964.

[70] B. R. Brown and A. Lohmann, “Computer - generated binary holograms,” *IBM Journal of Research and Development* **13**, pp. 160–168, 1968.

[71] A. W.Lohmann and D.P.Paris, “Binary fraunhofer holograms, generated by computer,” *Appl. Opt* **6**, p. 1739, 1967.

[72] L. B. Lesem, P. Hirsch, and J. J. Jr, “The kinoform: A new wave front reconstruction device,” *IBM* **13**, pp. 150–155, 1969.

[73] J. R. M. Cessa, *Design and fabrication of Holographic Optical Elements and Kin oforms.* PhD thesis, Centro de Investigaciones en Óptica, 1997.

[74] J. R. Fienup, “Phase retrieval algorithms: a comparison,” *Appl. Opt* **21**, p. 2758, 1982.

[75] B. R. Brown and A. W.Lohmann, "Complex spatial filtering with binary mask," *Appl. Opt.* **5**(6), pp. 967 – 969, 1966.

[76] J. M. Huntley and H. Saldner, "Error - reduction methods for shape measurement by temporal phase unwrapping," *JOSA A* **14**, pp. 3188–3196, 1997.

[77] C. A. Gonzalez, A. Davila, and J. G. Garnica, "Noise reduction of temporal phase unwrapping for 3d shape reconstruction using a quality map," in *Sixth Symposium Optics in Industry*, J. C. Gutierrez-Vega, J. Davila-Rodriguez, and C. Lopez-Mariscal, eds., *Proc. SPIE* **6422**, 2007.

[78] K. T. Gribbon, C. Johnston, and D. Bailey., "A real - time fpga implementation of a barrel distortion correction algorithm with bilinear interpolation," in *Image and Vision Computing '03 NZ*, D. D. Bailey, ed., *IVCNZ 2003*, pp. 408–413, 2003.

[79] M. Takeda and K. Mutoh, "Fourier transform profilometry for the automatic measurement of 3d objects shapes," *Appl. Opt.* **22**, pp. 3977–3982, 1983.

[80] V. Srinivasan, H. Liu, and M. Halioua, "Automated phase-measuring profilometry of 3d diffuse objects," *Appl. Opt.* **23**, pp. 3105–3108, 1984.

[81] S. Toyooka and I. Iwaasa, "Automatic profilometry of 3d diffuse objects by spatial phase detection," *Appl. Opt.* **24**, pp. 1630–1633, 1986.

[82] K. J. Gasvik, *Optical Metrology*, John wiley & Sons, 2002.

[83] C. Soutar, S. E. M. Jr., and J. Knopp, "Measurement of the complex transmittance of the epson liquid crystal television," *Opt. Eng.* **33**, pp. 1061–1068, 1994.

[84] H. Zhang, J. Zhang, and L. Wu, "Evaluation of phase only liquid crystal spatial light modulator for phase modulation performance using a twyman-green interferometer," *IOP Measurement Science and Technology* **18**, pp. 1724–1728, 2007.

[85] H. Dai, K. X. Y. Liu, X. Wang, and J. Liu, "Characteristics of lcos phase only spatial light modulator and its applications," *Opt. Commun.* **238**, pp. 269–276, 2004.

[86] S. of Photo Instrumentation Engineers, ed., *Improving spatial light modulator performance through phase compensation*, (5553), (Boulder Nonlinear System Inc. 450 Courtney Way 107 Lafayette Coorado), SPIE, 2004.

[87] Casasent, D. P, Chao, and Tien-Hsin, eds., *High resolution phase only spatial light modulators with sub-millisecond response*, (5106), SPIE, SPIE, 2003.

[88] A. Marquez, C. Iemmi, I. Moreno, J. A. Davis, J. Campos, and M. J. Yzuel, "Quantitative prediction of the modulation behavior of twisted nematic liquid crystal displays based on a simple physical model," *Opt. Eng* **40**, pp. 2558 – 2564, 2001.

[89] A. Marquez, C. Iemmi, I. Moreno, J. Campos, and M. J. Yzuel, "Anamorphic and spatial frequency dependent phase modulation on liquid crystal display. optimization of the modulation diffraction," *Optics Express* **13**, pp. 2111–2119, 2005.

[90] J. Nicolas, J. Campos, and M. J. Yzuel, "Phase and amplitude modulation of elliptic polarization states by nonabsorbing anisotropic elements: application to liquid crystal devices," *JOSA A.* **19**, pp. 1013 – 1020, May 2002.

[91] A. Marquez, J. Campos, M. J. Yzuel, I. Moreno, J. A. Davis, C. Iemmi, A. Moreno, and A. Robert, "Characterization of edge effects in twisted nematic liquid crystal displays," *Opt. Eng.* **39**, pp. 3301–3307, 2000.

[92] G. Cristobal, B. Javidi, and S. Vallmitjana, eds., *Simple Jones Method for describing Modulation Properties of Reflective Liquid Crystal Spatial Light Modulators*, (860), American Institute pf Physics, Information Optics: 5th International Workshop, 2006.

[93] H. Huan, O. Sasaki, and T. Susuki, "Multiperiod fringe projection interferometry sing a back propagation method for surface profile measurement," *Appl. Opt.* **46**, pp. 7268–7274, 2007.

[94] F. Yang and X. He, "Two step phase shifting fringe projection profilometry intensity derivative approach," *Appl. Opt.* **46**, pp. 7172–7178, 2007.

[95] 3dshape, November 2007. `http://www.3d-shape.com/home/home_d.php`.

[96] P. Vision, November 2007. `http://www.phasevision.co.uk/`.

[97] Creaform3d, November 2007. `http://www.creaform3d.com/`.

[98] A. Martinez, R. R. Vera, J. A. Rayas, and J. F. Vazquez, "Influence of object roughness on specimen gratings for moire interferometry," *Opt. Eng.* **40**, pp. 1978–1983, 2001.

[99] F. J. Cuevas, J. H. S. Azuela, and M. Servin, "A parametric method applied to phase recovery from a fringe pattern based on genetic algorithm," *Opt. Commun.* **203**, pp. 213–223, 2002.

[100] H. O. Saldner and J. M. Huntly, "Profilometry using temporal phase unwrapping and a spatial light modulator - based fringe," *Opt. Eng.* **36**, pp. 610–615, 1997.

[101] H. Du and Z. Wang, “Three dimensional shape measurement with an arbitrary arranged fringe projection profilometry system,” *Opt. Lett* **32**, pp. 2438–2440, 2007.

Appendix A

Intensity Calibration

LCoS are extensively used in areas as optical diffractive elements, in adaptive optics and image processing. In all these areas, it is desirable a high contrast amplitude modulation, more over the phase stepping equation mathematically assumes that the fringe pattern projected over the specimen and then captured by the camera have a pure sinusoidal intensity. Therefore, the need to characterize the LCoS behavior is an important task. There are many works about liquid crystal calibration, most of them measure the complex transmittance and the properties of phase modulation[13, 25, 92].

The LCoS produce a pair of amplitude and phase modulation of reflected light as a function of an applied voltage[91], the modulation produced by the LCoS over the reflected light is a function of the twist angle and the birefringence of the liquid crystal, this is because when a voltage is applied the liquid crystal molecules tilt toward the electric field direction changing the amplitude and phase modulation. The optical setup used in the calibration procedure is showed in Fig. A.1, which is a simple adaptation from other experiments used in transmissive liquid crystal display[88, 90, 83]. Light linearly-polarized from a HeNe laser (633 nm-35 mW) arrives to the LCoS by the use of a non polarizer beamsplitter, a video signal with a gray constant level over the whole field is used as input for the LCoS, the signal is increased from 0 to 255, the LCoS reflected light pass through the beamsplitter and the polarizer. The

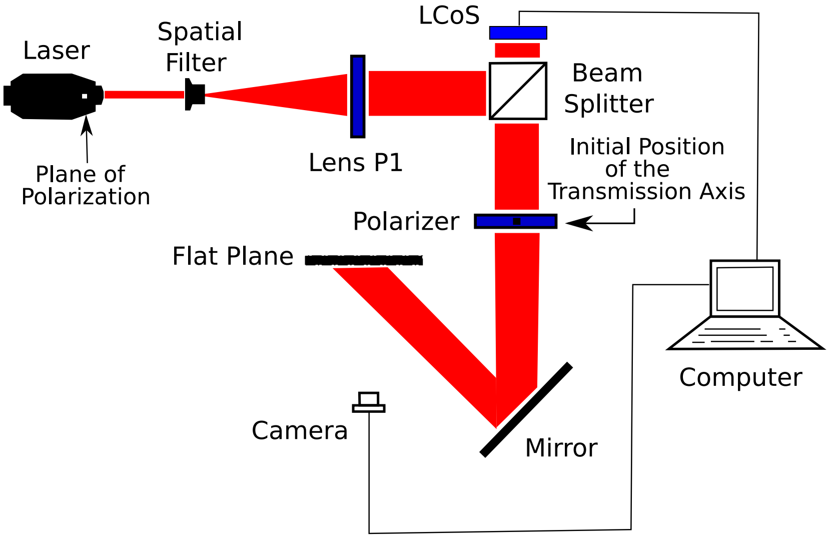

Figure A.1: Optical setup: A sequence of gray patterns (0-255) are projected for each position of the transmission axis of the polarizer, the camera acquires the resulting images.

camera acquires the resulting images from a flat white plane, this procedure is repeated for different orientations in the transmission axis of the polarizer.

A sequence of 256 gray levels, constant over the whole LCoS were projected by the optical system, each image corresponding to the gray level pass through the polarizer, as each gray level produce a particular phase modulation and complex amplitude, the intensity of the reflected light is a function of these two parameters and can be measured for each orientation of the polarizer as function of the gray level value, the results of this procedure are presented in Fig. A.2 which are similar to the results reported by Andres Marquez[91]. The final curve used in this calibration process, is showed in Fig. A.3 which can be considered in a specific region of gray levels projected [140 250] as a linear function.

The next step in our calibration procedure was to improve the contrast of the images acquired by the camera. Figure A.2 shows that the gray colors are mapped into a range of 25 gray levels, the optical setup is modified and

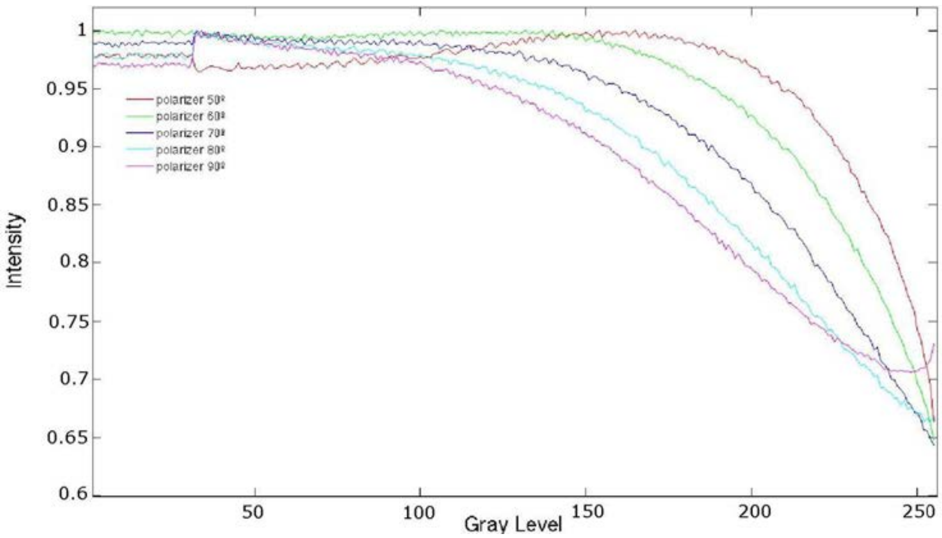

Figure A.2: Intensity reflectance versus the gray level for different orientations of the polarizer.

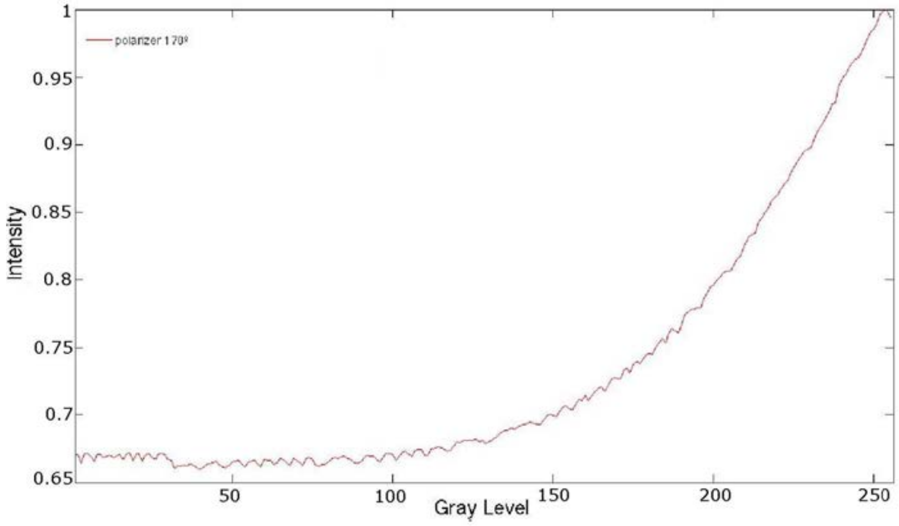

Figure A.3: Final result used from the calibration process. Intensity reflectance versus the gray level for different configurations of the polarizer.

now a polarizer beamsplitter replaces the polarizer in the optical setup. In general the sinusoidal fringe pattern digitalized by a camera can be described as[94, 80]:

$$I(x,y) = r(x,y)\left(a(x,y) + b(x,y)\sin(2\pi f x + \phi(x,y))\right) , \tag{A.1}$$

where $r(x,y)$ represents the object surface reflectivity, $a(x,y)$ represents the background, $b(x,y)$ is related to the fringe contrast, f is the spatial frequency, and $\phi(x,y)$ is the phase function to be determined and is related to the object shape; when the phase is extracted from Equation (A.1) it is necessary to consider that the roughness of the surface can be represented as a multiplicative noise, as it introduces some phase noise in the measurement. The process for increasing the contrast must take into account this factor, in order to increase the visibility of the fringe pattern acquired by the camera[27, 98]. Therefore, the noise can be reduced by manipulating the f-number of the lens camera. Figure A.4 shows the increased dynamic range obtained by changing the f-number of the camera lens.

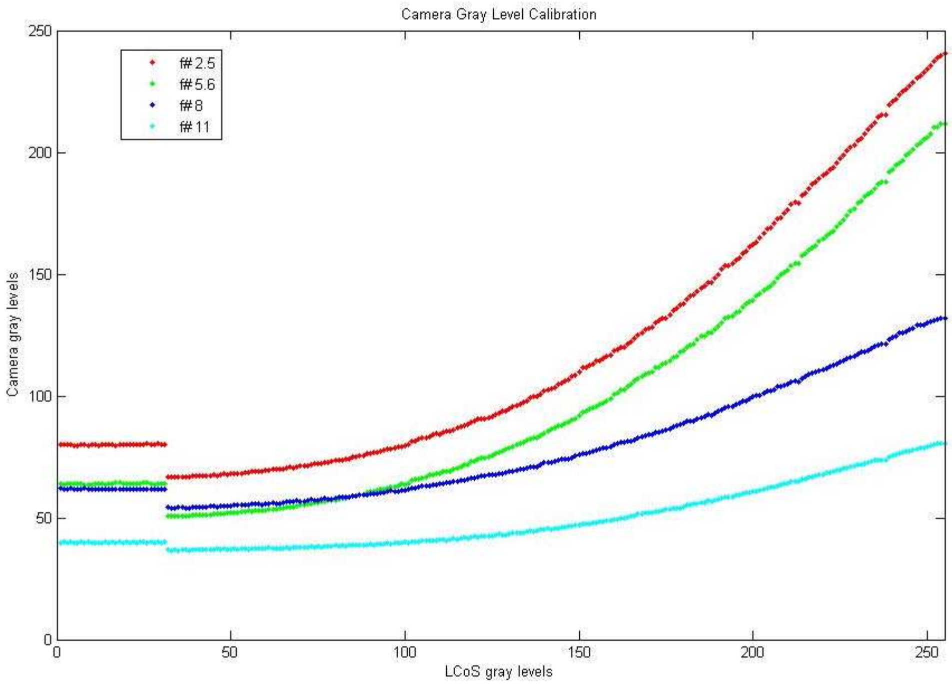

Figure A.4: Final result used from the calibration contrast process. Intensity reflectance versus the gray level projected by the LCoS. Different values of f number are used to average several speckles in a camera pixel, decreasing the noise in the acquired images

Appendix B

Spatial Calibration and Transformation from Phase to Real Units

A calibration procedure which avoid the need for distance measurements from the camera, projector and orientations is described by F. Cuevas[99], Saldner[100] and Hua Du[101]. In practice, the calibration system that uses the geometric measurements of the optical setup geometry are subject to uncertainties in physical measurements, as consequence the shape measurement accuracies are inevitably limited.

In principle, the calibration procedure was done using a glass flat plate mounted on a micrometer driven precision translation stage. The surface was painted by using spray paint with a thin layer of white matte color. The Z axis was set parallel to the normal of the surface, the plane was positioned in 10 different positions uniformly spaced in a volume of 2 cm, at each position an unwrapped phase map was obtained. Next, third order least square fit was applied to the points belonging to each pixel along of the Z axis, this calibration presents two principal problems. First, the mechanical elements used for alignment of the glass plate in order to have a vertical position without tilt, each time that this calibration procedure was applied a tilt in the flat

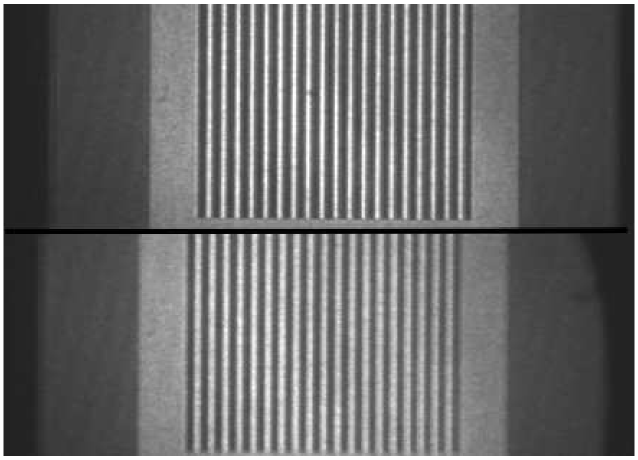

Figure B.1: Image of the projection area displacement, the top figure shows the area viewing by the camera in the first plane position, the second image below, shows the area viewing by the camera in the last plane position.

glass was present and hence the unwrapped phase maps include tilts errors. Secondly, the TPU algorithm assumes that each pixel of the projected fringe pattern does not move along the X or Y directions, this means that a camera pixel is seen as the same pixel along the Z axis. However this assumption does not hold in practice if a non-telecentric lens is used in the camera and because the projection angle also change along the Z axis.

Figure B.1 shows how the change of the projection angle moves a fringe pattern. the top figure correspond to the projection area at $Z = 0$, the second figure below shows the projection area at $Z = 2\ cm$.

In order to obtain a measurement of the resolution along the Z axis, we use calibrated metals gauges placed in a fan arrangement, the phase data obtained by this experiment allow us to create a lookup table giving a transformation among phase values and real units.

The result gave us a resolution in the range of $67\mu m$ for the smallest resolved step among to adjacent metal gauges. Figure B.2 and Figure B.3 show the 3D shape of the metal gauges and a profile along the X axis obtained by

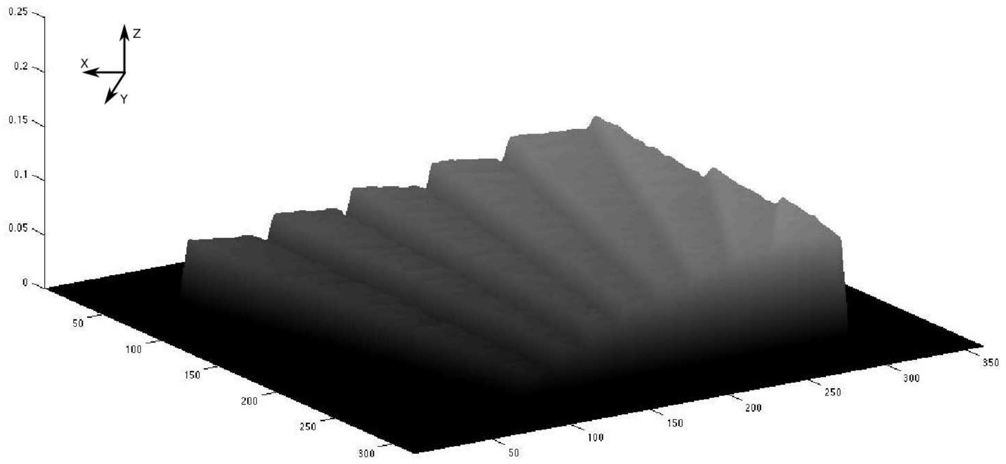

Figure B.2: 3D shape reconstruction of different metal gauges placed in a fan arrangement (scale in radians).

the proposed method.

The second calibration procedure to transform the 2D (X and Y) camera coordinates to spatial coordinates, this calibration procedure starts with the acquisition of an image produced by a grid of black square patterns into a white background as shown in Fig. B.4. In this grid we know the exact position of each square centroid, and we use this information to find out the possible image distortion. The centroid positions corresponding to the black squares were calculated using its first moment and compared to the corresponding position without distortion. Each comparison gave us two distortions along the horizontal and vertical directions, that we use to correct small distortions.

When the gear of Fig. 4.7 was used as specimen, the maximum distortions at the edge were found to be less than 4.5 pixels and corrected through a bilinear interpolation algorithm[78]. Although the projection area was only 2x2 black squares for the central area of the gear.

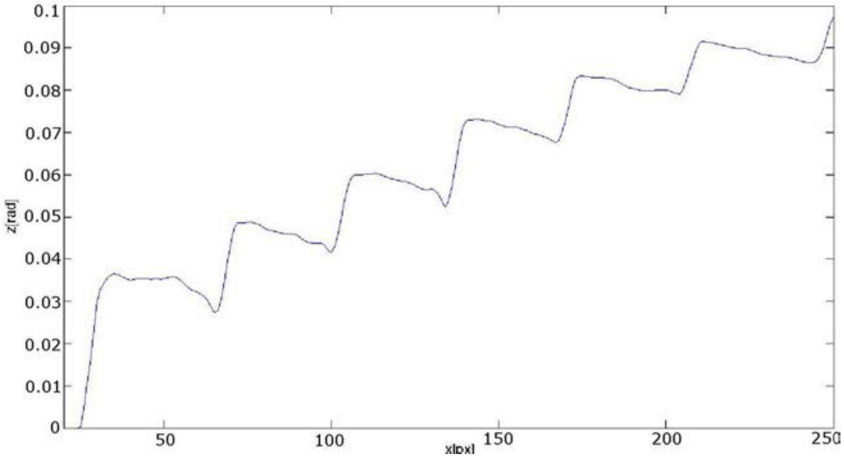

Figure B.3: Profile along the X axis of the 3D shape reconstruction Figure B.2 of the metal gauges.

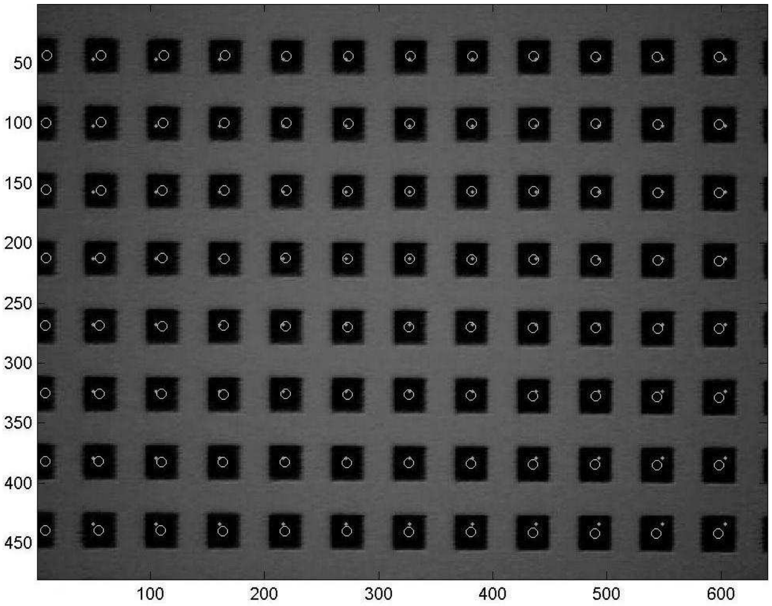

Figure B.4: First black squares moments used in the camera calibration pattern: circles indicate positions without distortion while dots indicate distortion. The first column of black squares from left to right was not considered in the calibration procedure (scale in pixels).